

Title	Scattering of carriers by coupled plasmon-phonon modes in bulk polar semiconductors and polar semiconductor heterostructures
Authors	Fahy, Stephen B.;Hauber, Anna
Publication date	2017-01-25
Original Citation	Hauber, A. and Fahy, S. (2017) 'Scattering of carriers by coupled plasmon-phonon modes in bulk polar semiconductors and polar semiconductor heterostructures', Physical Review B, 95(4), 045210 (29pp). doi:10.1103/PhysRevB.95.045210
Type of publication	Article (peer-reviewed)
Link to publisher's version	10.1103/PhysRevB.95.045210
Rights	© 2017 American Physical Society
Download date	2023-05-08 01:50:03
Item downloaded from	http://hdl.handle.net/10468/4953

Scattering of carriers by coupled plasmon-phonon modes in bulk polar semiconductors and polar semiconductor heterostructures

Anna Hauber^{*} and Stephen Fahy

*Tyndall National Institute, Lee Maltings, Dyke Parade, Cork, Ireland
and Department of Physics, University College Cork, Cork, Ireland*

(Received 5 February 2016; revised manuscript received 21 November 2016; published 25 January 2017)

We present a general treatment of carrier scattering by coupled phonon-plasmon collective modes in polar semiconductors, taking anharmonic phonon decay into account and self-consistently calculating carrier momentum relaxation rates and carrier mobility in a parabolic band model. We iteratively solve the weak-field Boltzmann equations for carriers and collective modes and obtain their nonequilibrium distribution functions. Both the scattering rates and the anharmonic decay of the coupled modes are expressed through the total dielectric function of the semiconductor, consisting of a damped lattice dielectric function, and a temperature dependent random phase approximation dielectric function for the carrier plasma. We show that the decay of the coupled modes has a significant effect on the contribution to the mobility limited by carrier-coupled mode scattering. We also propose a scalar quantity, the phonon dissipation weight factor, with which this effect can be estimated from an analytic expression. We apply this treatment to dynamically screened electron-longitudinal optical phonon scattering in bulk polar semiconductors, and to dynamically screened remote phonon scattering in polar heterostructures where monolayers of MoS₂ are sandwiched between various polar dielectrics. We find that a dynamic treatment of the remote phonon scattering yields mobilities up to 75% higher than a static screening approximation does for structures which consist of a monolayer of MoS₂ between hafnia and silica. Moreover, we show that accounting for the nonzero thickness of the MoS₂ interface layer has an important effect on the calculated mobility in the same structure.

DOI: [10.1103/PhysRevB.95.045210](https://doi.org/10.1103/PhysRevB.95.045210)

I. INTRODUCTION

Polar semiconductors play an important role in several fields of semiconductor technology today. They are used in LEDs and semiconductor lasers, as they are optically active. Certain polar semiconductors, like lead telluride alloys, also show thermal properties which are promising for energy harvesting [1]. Perhaps technologically most importantly, metal-oxide-semiconductor field effect transistors (MOSFETs) with a polar dielectric as a gate oxide and a semiconducting channel, are polar semiconductor devices and form the basis of modern electronics. In current MOSFETs, high- κ dielectrics are usually grown on silicon. But even new, more experimental MOSFETs cannot forgo the polar dielectric, e.g., in the recent MOSFETs consisting of a monolayer of molybdenite [2] on silica [3]. For all these applications, the understanding of carrier transport in highly doped polar semiconductors is vital.

In many applications, semiconductors are highly doped or photoexcited [4,5] to increase the carrier concentration, so that the high number of charge carriers delocalized throughout the semiconductor form a plasma. In nonpolar semiconductors, natural, unforced longitudinal oscillations of this plasma occur at the plasma frequency.

In polar semiconductors, the lattice can also cause a polarization field, when the different species of atoms oscillate out of phase. The corresponding natural longitudinal excitations occur at longitudinal optical (LO) phonon frequencies. Highly doped polar semiconductors have both a carrier plasma and optically active lattice excitations, which couple through their depolarization fields. We will be concerned with these coupled

collective excitations of the lattice and the carrier plasma throughout this paper, and we will simply call them “coupled modes” in the following.

In the semiconductor heterostructures consisting of MoS₂ sandwiched between different polar dielectrics, which we investigate in this paper, each of the constituent layers on its own has at least one longitudinal optical phonon mode. They all couple with each other and with the carriers in MoS₂ monolayer, yielding a complicated spectrum of coupled modes.

As the longitudinal optical excitations in highly doped polar semiconductors are coupled with the plasma excitations, carrier scattering in such materials cannot be modeled by independent carrier-LO-phonon scattering and carrier-carrier scattering. Carrier-LO-phonon scattering is known to have an important effect on the carrier mobility [see Ref. [6] for a comparison of the different scattering mechanisms in gallium arsenide (GaAs)]. Carrier-carrier scattering, which can be considered as carrier-plasmon scattering [7] to make direct comparison with carrier-phonon scattering easier, is usually assumed to have a negligible effect on the mobility, see, e.g., the discussion in Ziman’s textbook [8]. In highly doped polar semiconductors, the plasma frequency can be large enough to be comparable to the LO-phonon frequencies, and the coupled mode frequencies differ significantly from both the plasma and LO-phonon frequencies, as has been measured for bulk PbTe [9] following calculations by Varga [10]. Therefore carrier scattering with the coupled modes needs to be investigated carefully. It cannot be assumed a priori that either carrier LO-phonon or carrier plasmon scattering describe it accurately.

This paper proposes a method that treats the scattering of carriers by coupled excitations in a generalized way, and on

^{*}a.hauber@umail.ucc.ie

an equal footing. To stress this, we coin the phrase “coupled collective mode scattering” for what is usually called “screened LO-phonon scattering.” Our treatment includes LO-phonon scattering and carrier-carrier scattering as limiting cases.

We also introduce a quantity which we shall call the “phonon dissipation weight factor,” which arises naturally in the formalism and which characterizes how strongly scattering with a coupled excitation contributes to degrading an electric current on a scale from zero to one. Zero—no degradation of the current—corresponds to the conventional description of carrier-carrier scattering, and one characterizes the LO-phonon scattering limit. Thus the phonon dissipation weight factor provides some intuitive measure of the character of the coupled excitations and as such is related, although not identical, to the “phonon content” described by other authors [10–13].

It is well known that LO-phonons and plasmons in doped polar semiconductors are coupled [9,10,14], but the effect of this coupling on momentum relaxation has been less clear. Varga [10] gave the frequencies of the resulting coupled excitations in the long-wavelength limit, and also defined their “phonon content”—the part of the total kinetic energy which is due to the lattice. Ridley used the phonon content to derive the scattering rate of the coupled modes in the long-wavelength limit [12]. He also commented that this was equivalent to the expression of Kim *et al.* [11], where the scattering rate is calculated from the dielectric function of the coupled plasma-lattice system. While Kim’s long-wavelength expression is satisfactory for the scattering rate and the energy relaxation rate, this is not true for the momentum relaxation rate.

In their calculations of carrier mobility in MOSFETs, Fischetti *et al.* [13] were aware of this problem, and alleviated it by taking into account what they called “an approximate treatment of Landau damping.”¹ They used the long-wavelength limit expression for the coupled mode momentum relaxation rate only up to a certain cutoff wave vector, and the LO-phonon momentum relaxation rate for larger wave vectors. This provided a patch to the problem, and was suitable to the realistic device-physics application they studied. However, Fischetti *et al.* [13] did not publish an investigation of the validity of their approximation. We will carry out a careful assessment of their approximation in this work.

The scattering rate calculated from the dielectric function by Kim *et al.* [11] can describe finite wave-vector effects by taking the wave-vector dependence of the dielectric function into account. Using the zero-temperature random-phase approximation (RPA) dielectric function [15] for the electronic dielectric function and a Lyddane-Sachs-Teller [16] type lattice dielectric function as suggested by Varga [10], Kim *et al.* [11] could calculate the changes in the coupled mode excitation frequencies as a function of wave vector [11].

Sanborn [7] expands on the method by Kim *et al.* [11] by using scattering rates calculated from the dielectric function in a Boltzmann transport equation to find the momentum relaxation rates. A variety of scattering mechanisms enter

Sanborn’s numerical calculations of momentum relaxation rates in GaAs [17], which makes it difficult to track the effect of carrier-coupled mode scattering specifically. However, the structure of her electron-electron collisional integral shows that they reproduce the textbook result [18] that electron-electron scattering in parabolic bands does not degrade an electric current. Sanborn’s electron-electron scattering model can be extended to the case of carrier—coupled mode scattering. Yet, Sanborn stopped short of doing this, but used an approximate treatment of the carrier-coupled mode scattering in another collisional integral in the Boltzmann equation. The present work generalizes Sanborn’s approach to include carrier-coupled mode scattering.

Our contribution, the critical step to the generalization of carrier-carrier scattering to carrier-coupled mode scattering, is to realize the importance of the collective mode decay mechanism for momentum relaxation. We formulate a Boltzmann equation for the carriers—including a term due to the external electric field, and a Boltzmann equation for the coupled excitations, including the anharmonic decay of the LO-phonons. We find that the details of the anharmonic decay determines how far the coupled excitations are out of equilibrium²—this is analogous to the phonon drag effect [8]. This in turn affects the carrier contribution to the momentum relaxation, and hence the carrier mobility.

We first apply our approach to a series of bulk polar semiconductors where electron-LO-phonon scattering is well described with electrons in a single spherical, parabolic conduction band interacting with a single LO-phonon resonance. This simple case allows us to develop qualitative understanding of coupled collective mode scattering, which we can carry over to our investigation of screened interface phonon scattering (also called “remote phonon” or “surface optical phonon” scattering) [13,19] in polar semiconductor heterostructures. Drawing on work by Maslov [20] and Stern [21], we can apply our treatment of coupled collective mode scattering to interface phonon scattering, directly after finding an effective scalar dielectric function for the investigated semiconductor heterostructure.

MoS₂ has attracted great interest in the last several years, because single atomic layers of it can be exfoliated [2]. As a semiconductor, a gap is already present in its band structure [22,23] and does not have to be painstakingly introduced before it comes suitable for electronic applications. Field-effect transistors with one or few layers of MoS₂ as the channel material have already been realized [3,24]. Such devices have the advantage of eliminating carrier scattering due to surface roughness [25]. As there are two equivalent conduction band minima with quite high effective mass in monolayer MoS₂, screening effects are important [23,25,26]. If defects in the MoS₂ layers, which presently limit the carrier mobility through large charged impurity scattering [27,28], can be decreased, higher carrier mobilities could be reached. Therefore a careful investigation of dynamically screened interface polar phonon scattering is of interest. As the conduction band minima in monolayer MoS₂ are well

¹Note that Landau damping was originally introduced in the classical limit [39] and not in the extreme quantum limit, as used by Ref. [13].

²Sanborn [7] implicitly assumed that the LO-phonon distribution function, not the plasmon distribution function, is in equilibrium.

described by spherical parabolic bands and well separated in energy from the next lowest conduction band extrema [23,29], we will follow Refs. [25,27,29] in treating transport in MoS₂ with effective mass theory.

This paper is organized as follows. In Sec. II, we discuss coupled linearized Boltzmann equations for both the carriers and the coupled collective modes and present our self-consistent solution. In Sec. III, we apply this to bulk polar semiconductors. In Sec. IV, we derive a scalar effective dielectric function for a polar semiconductor heterostructure, which allows us to apply our treatment of coupled collective mode scattering to screened interface phonon scattering. In Sec. V, we apply this to polar semiconductor heterostructures which consist of MoS₂ between different polar dielectrics. Section VI gives a summary and some conclusions. In Appendix A, we relate our approach to the existing treatment of coupled modes [10–13] by reviewing some important limiting cases. Appendix B explains how we iterate the effective momentum relaxation time to self-consistency. Appendix C gives explicit expressions for the effective momentum relaxation time for bulk semiconductors with spherical parabolic bands. Appendix D gives the corresponding expressions for two-dimensional polar semiconductors. Appendix E reviews other intrinsic scattering mechanisms in polar heterostructures with a molybdenite monolayer as the channel.

II. COUPLED BOLTZMANN EQUATIONS FOR CARRIERS AND COLLECTIVE MODES

The coupled Boltzmann equations for carriers and phonons can be found in many textbooks. We follow the description by Peierls [[18], Chap. 6], using the notation from Pines' textbook [[30], Chap. 5]. However, we apply Peierls's phonon Boltzmann equation to all collective modes of the coupled phonon-plasmon system. Therefore we have to extend Peierls's formalism from discrete modes to allow for a continuous spectrum of collective modes at each wave vector.

Our model incorporates three distinct effects. Firstly, the carriers and the collective excitations interact with each other. The carriers are either electrons or holes, and for the cases investigated in this paper, we can imagine that their wave vectors are close to one or several equivalent band extrema, though we will only specify the exact expressions in Appendixes C and D. The collective excitations are either one or more longitudinal optical phonons, or plasma excitations, or, in general, coupled plasmon-LO-phonon modes. Secondly, the carriers are accelerated by an external electric field. Thirdly, the collective excitations can decay. The decay will be different for phonons, plasmons, and coupled phonon-plasmon excitations. In our model, the interaction between the collective modes and the carriers, and the decay of the collective modes are quantified through dielectric functions. We will illustrate this for the example of carrier-LO-phonon scattering throughout this section, making use of the dielectric functions for damped LO-phonons

$$\varepsilon_{\omega}^{\text{ph}} = \varepsilon^{\infty} + \frac{\varepsilon^0 - \varepsilon^{\infty}}{1 - \frac{\omega^2}{\omega_{\text{TO}}^2} - i \frac{\omega\gamma}{\omega_{\text{TO}}^2}}. \quad (1)$$

We find the mobility of the carriers by solving the coupled Boltzmann equations self-consistently for both the distribution function $f_{\mathbf{p}}$ of a carrier of wave vector \mathbf{p} and the distribution function $N_{\mathbf{k},\omega}$ of a collective mode of wave vector \mathbf{k} and frequency ω . We do this in the weak-field approximation.

A. Linearized Boltzmann equations for the weak field limit

The issue in solving the coupled Boltzmann equations is that both the distribution functions $N_{\mathbf{k},\omega}$ and $f_{\mathbf{p}}$ and the scattering rate $W_{\mathbf{k},\omega}$ are unknown. All we have are their equilibrium values: $N_{\mathbf{k},\omega}^0$, the Bose-Einstein distribution function, $f_{\mathbf{p}}^0$, the Fermi-Dirac distribution function, and $W_{\mathbf{k},\omega}^0$, the equilibrium scattering rate, which will be discussed in Sec. II B 2. In the case where the field is small enough to drive the system only slightly out of equilibrium, we can linearize the Boltzmann equations around the equilibrium expressions. This gives us equations featuring the familiar equilibrium values $N_{\mathbf{k},\omega}^0$, $f_{\mathbf{p}}^0$, and $W_{\mathbf{k},\omega}^0$, which we subsequently solve for the small deviations g and G of the distributions from their equilibrium values. All first-order terms will be denoted by the superscript 1, and all equilibrium, or zeroth-order terms by the superscript 0.

We use Peierls's notation [18] for the linearized distribution function of the carriers of wave vector \mathbf{p} ,

$$f_{\mathbf{p}}^1 = f_{\mathbf{p}}^0 - g_{\mathbf{p}} \frac{\partial f_{\mathbf{p}}^0}{\partial E_{\mathbf{p}}} = f_{\mathbf{p}}^0 + f_{\mathbf{p}}^0 (1 - f_{\mathbf{p}}^0) \beta g_{\mathbf{p}}, \quad (2)$$

and the linearized distribution function of a collective mode σ and wave vector \mathbf{k} :

$$\begin{aligned} N_{\mathbf{k},\sigma}^1 &= N_{\mathbf{k},\sigma}^0 - G_{\mathbf{k},\sigma} \frac{\partial N_{\mathbf{k},\sigma}^0}{\partial \hbar \omega_{\mathbf{k},\sigma}} \\ &= N_{\mathbf{k},\sigma}^0 + N_{\mathbf{k},\sigma}^0 (1 + N_{\mathbf{k},\sigma}^0) \beta G_{\mathbf{k},\sigma}. \end{aligned} \quad (3)$$

Here, $\beta = \frac{1}{k_B T}$ with the temperature T and the Boltzmann constant k_B . $\hbar \omega_{\mathbf{k},\sigma}$ is the energy of a mode (\mathbf{k}, σ) . The collective mode index is $|\sigma| \in \{1, \dots, \Sigma\}$, where Σ is the number of discrete modes. $E_{\mathbf{p}}$ is the kinetic energy of a carrier with wave vector \mathbf{p} . We assume that $\beta G_{\mathbf{k},\sigma} \ll N_{\mathbf{k},\sigma}^0$ and $\beta g_{\mathbf{p}} \ll f_{\mathbf{p}}^0$.

B. Carrier Boltzmann equation

As we are interested in a stationary, homogeneous solution to the carrier Boltzmann equation, only the field term and the collision term are nonvanishing. Hence the Boltzmann equation for the carriers states that the change of the distribution $f_{\mathbf{p}}$ of carriers of wave vector \mathbf{p} due to the electric field is balanced by its change due to collisions with collective excitations:

$$\left(\frac{\partial f_{\mathbf{p}}}{\partial t} \right)_{\text{field}} = \left(\frac{\partial f_{\mathbf{p}}}{\partial t} \right)_{\text{coll}}. \quad (4)$$

In our semiclassical picture, we can use Newton's second law for the change in wave vector due to the force $e\mathbf{E}$ caused by the external electric field \mathbf{E} , yielding, to first order the field term

$$\left(\frac{\partial f_{\mathbf{p}}}{\partial \mathbf{p}} \cdot \frac{e\mathbf{E}}{\hbar} \right)^1 = \frac{\partial f_{\mathbf{p}}^0}{\partial \mathbf{p}} \cdot \frac{e\mathbf{E}}{\hbar} = -\beta f_{\mathbf{p}}^0 (1 - f_{\mathbf{p}}^0) \mathbf{v}_{\mathbf{p}} \cdot e\mathbf{E}, \quad (5)$$

where $\mathbf{v}_{\mathbf{p}} = \frac{1}{\hbar} \frac{\partial E_{\mathbf{p}}}{\partial \mathbf{p}}$ is the group velocity.

Peierls's carrier collision term in the Boltzmann equation [18] is

$$\begin{aligned} \left(\frac{\partial f_p}{\partial t} \right)_{\text{coll}}^1 &= \int_k \sum_{\sigma} 2\pi F_k^{\sigma} \delta(E_{p+k} - E_p - \hbar\omega_{k,\sigma}) \\ &\quad \times f_{E_{p+k}}^0 (1 - f_{E_p}^0) \beta (N_{k,\sigma}^0 + 1) \\ &\quad \times (g_{p+k} - g_p - G_{k,\sigma}) \end{aligned} \quad (6)$$

to first order in our notation. δ is the Dirac delta function and enforces energy conservation. The conservation of crystal momentum is already built into the expression. We use Peierls's short convention [18], where negative values of σ mean a negative transferred energy $\hbar\omega_{k,-|\sigma|} = -\hbar|\omega_{k,|\sigma|}|$. The symbol \int_k signifies a d -dimensional integration over all collective mode states \mathbf{k} . We show how this is parametrized in practice for two and three dimensional semiconductors in Appendix C.

F_k^{σ} is the scattering strength for a carrier scattering with a collective mode (\mathbf{k}, σ) in equilibrium, and will be discussed in Sec. II B 2, and in Appendix A. For scattering between carriers and undamped LO-phonons, for example, the scattering strength is given by Eq. (A6), and can be derived from the scattering matrix element squared of the Fröhlich Hamilton. We will use a different derivation, relying on the dielectric function rather than the Hamiltonian of the system. We also assume that F_k^{σ} only depends on the transferred wave vector \mathbf{k} , and not on the initial and final wave vectors \mathbf{p} and $\mathbf{p} + \mathbf{k}$. We will discuss the validity of this assumption for the cases discussed in this paper at the beginning of Sec. III.

1. Continuous modes

Up to now, we have not accounted for the possibility of the collective modes being damped. The collective modes had infinitely sharp excitations at discrete frequencies. From now on, we describe them with the Lorentzian $D_{k,\omega}^{\sigma}$ whose width and height is determined by the lifetime of the collective mode.

For such damped modes, we have to blur out the energy conservation by replacing the delta function $\delta(E_{p+k} - E_p - \hbar\omega_{k,\sigma})$ in Eq. (6) with the Lorentzian $D_{k,\omega}^{\sigma}$. This can be written by multiplying the right-hand side (r.h.s.) of Eq. (6) by the Lorentzian $D_{k,\omega}^{\sigma}$, indexing the collective mode distribution function with their frequency $\omega_{k,\sigma}$ rather than their mode number σ ,

$$N_{k,\sigma}^0 \rightarrow N_{k,\omega}^0 \quad \text{and} \quad G_{k,\sigma} \rightarrow G_{k,\omega}, \quad (7)$$

and integrating over the new continuous frequency variable ω . This yields

$$\begin{aligned} \left(\frac{\partial f_p}{\partial t} \right)_{\text{coll}}^1 &= \int_k \int_{\hbar\omega} W_{k,\omega}^0 \delta(E_{p+k} - E_p - \hbar\omega) \\ &\quad \times f_{E_{p+k}}^0 (1 - f_{E_p}^0) \beta (N_{k,\omega}^0 + 1) \\ &\quad \times (g_{p+k} - g_p - G_{k,\omega}), \end{aligned} \quad (8)$$

where we have defined the new equilibrium scattering rate

$$W_{k,\omega}^0 = \sum_{\sigma} \frac{2\pi}{\hbar} F_k^{\sigma} D_{k,\omega}^{\sigma}, \quad (9)$$

which gives the probability per unit time and unit reciprocal space that a scattering event between a continuous collective mode at the frequency ω and wave vector \mathbf{k} occurs. Equation (9) shows that $W_{k,\omega}^0$ depends on the damping and the scattering strength of all modes σ . If $D_{k,\omega}^{\sigma}$ is a series of delta peaks [cf. Eq. (A2)], Eq. (8) reduces to Eq. (6).

2. Equilibrium scattering rate $W_{k,\omega}^0$ from the dielectric function

Rather than calculating the scattering strengths of the collective modes from the Hamiltonian of the system and taking the lifetime into account through a blurred energy conservation relation, we will express the equilibrium scattering rate directly from the dielectric function of the system. As described in Chap. 2.6 of Ref. [31], using Fermi's golden rule and the dissipation-fluctuation theorem [32,33], we can express the equilibrium scattering rate through the dielectric function of the system as

$$W_{k,\omega}^0 = \frac{2\nu_k}{\hbar} \Im \left(\frac{-1}{\epsilon_{k,\omega}^{\text{tot}}} \right). \quad (10)$$

We also introduced ν_k , the Fourier transform of the Coulomb potential, which is

$$\nu_k = \begin{cases} \frac{2\pi e^2}{k} & \text{dimension } d = 2, \\ \frac{4\pi e^2}{k^2} & \text{dimension } d = 3. \end{cases} \quad (11)$$

For carrier-LO-phonon scattering, e.g., Eq. (10) becomes $W_{k,\omega}^0 = \frac{2\nu_k}{\hbar} \Im \left(\frac{-1}{\epsilon_{k,\omega}^{\text{ph}}} \right)$ with the dielectric function Eq. (1) and Eq. (9) becomes $W_{k,\omega}^0 = F_k^u (D_{\omega}^u - D_{-\omega}^u)$ with F_k^u from Eq. (A6) and

$$\mathfrak{D}_{\omega}^u = \frac{\omega_{\text{LO}}}{\sqrt{\omega_{\text{LO}}^2 - (\frac{\gamma}{2})^2}} \frac{\frac{1}{\pi} \frac{\gamma}{2}}{(\omega - \sqrt{\omega_{\text{LO}}^2 - (\frac{\gamma}{2})^2})^2 + (\frac{\gamma}{2})^2}.$$

It can be shown with elementary algebra that Eqs. (10) and (9) are equivalent for carrier-LO-phonon scattering.

Equation (10) has been used for homogeneous electron systems [31], but also for systems with coupled electrons and polar phonons [11], where the electrons are treated in the random phase approximation (RPA) [30] and the phonons in the long-wavelength limit. Note that, in Peierls's convention, $W_{k,-\omega}^0 = -W_{k,\omega}^0$, yet the product $W_{k,-\omega}^0 (N_{k,-\omega}^0 + 1) = W_{k,\omega}^0 N_{k,\omega}^0$ is always positive, because the frequencies ω and hence the distribution functions N_{ω}^0 are allowed to be negative. This way, we can write the collisional term (8) with an integral over positive and negative frequencies, which saves us separate terms for the emission and absorption of a coupled collective mode of positive frequency.

It is important to realize that notation for the scattering rate is not consistent across the literature, and it is particularly vital not to mistake the scattering rate, $W_{k,\omega}^0$ defined in Eq. (10), with the momentum relaxation rate discussed in Sec. II D, or the energy relaxation rate.

C. Collective mode Boltzmann equation

The stationary Boltzmann equation for the collective excitations requires that the change of the distribution $N_{k,\sigma}$ due to collisions with carriers is balanced by the decay due to

anharmonic coupling:

$$\left(\frac{\partial N_{k,\sigma}}{\partial t}\right)_{\text{coll}} + \left(\frac{\partial N_{k,\sigma}}{\partial t}\right)_{\text{decay}} = 0. \quad (12)$$

We assume that the rate of decay of the collective mode (\mathbf{k}, σ) due to anharmonic processes is proportional to the deviation $\Delta N_{k,\sigma}$ of the distribution function from its equilibrium value. We will allow the constant of proportionality, the relaxation time $\tau_{k,\sigma}$ to depend on (\mathbf{k}, σ) . We will specify the exact form of $\tau_{k,\sigma}$ later in this section:

$$\left(\frac{\partial N_{k,\sigma}}{\partial t}\right)_{\text{decay}} = -\frac{\Delta N_{k,\sigma}}{\tau_{k,\sigma}}. \quad (13)$$

To first order, the deviation of the distribution function of the collective excitation from its equilibrium value is $\Delta N_{k,\sigma} = N_{k,\sigma}^0(1 + N_{k,\sigma}^0)\beta G_{k,\sigma}$, so that

$$\left(\frac{\partial N_{k,\sigma}}{\partial t}\right)_{\text{decay}}^1 = -\frac{N_{k,\sigma}^0(1 + N_{k,\sigma}^0)\beta G_{k,\sigma}}{\tau_{k,\sigma}}. \quad (14)$$

The collisional integral for the collective mode σ to first order is

$$\begin{aligned} \left(\frac{\partial N_{k,\sigma}}{\partial t}\right)_{\text{coll}}^1 &= 2 \int_p 2\pi F_k^\sigma \delta(E_{p+k} - E_p - \hbar\omega_{k,\sigma}) \\ &\quad \times (f_{E_p}^0 - f_{E_{p+k}}^0) \beta N_{k,\sigma}^0 (N_{k,\sigma}^0 + 1) \\ &\quad \times (g_{p+k} - g_p - G_{k,\sigma}) \end{aligned} \quad (15)$$

(see, e.g., Refs. [18,30]). The factor 2 accounts for the spin degeneracy. Note that the integrand on the r.h.s. of Eq. (15) is identical to the integrand on the r.h.s. of Eq. (6) for the rate of change of the carrier distribution function.

1. Solution for the collective mode Boltzmann equation

We now solve the collective mode Boltzmann equation (12) in its linearized form for the nonequilibrium distribution $G_{k,\sigma}$,

$$\begin{aligned} G_{k,\sigma} &= \frac{4\pi F_k^\sigma \int_p \delta(E_{p+k} - E_p - \hbar\omega_{k,\sigma}) (f_{E_p}^0 - f_{E_{p+k}}^0) (g_{p+k} - g_p)}{\frac{1}{\tau_{k,\sigma}} + \frac{2F_k^\sigma}{v_k} \Im(\varepsilon_{k,\omega_{k,\sigma}}^c)}. \end{aligned} \quad (16)$$

We simplified the second term in the denominator of Eq. (16) by using

$$\Im(\varepsilon_{k,\omega}^c) = 2\pi v_k \int_p \delta(E_{p+k} - E_p - \hbar\omega) (f_{E_p}^0 - f_{E_{p+k}}^0), \quad (17)$$

the definition of the imaginary part of the carrier dielectric function $\Im(\varepsilon_{k,\omega}^c)$ in the random phase approximation (RPA) [[30], Chap. 3].

The first term in the denominator on the r.h.s of Eq. (16) is (by definition) the fractional rate at which energy is dissipated from a mode (\mathbf{k}, σ) , due to anharmonic decay,

$$1/\tau_{k,\sigma}^{\text{coupled-ph}} = -\left(\frac{\partial U_{k,\sigma}}{\partial t}\right)^{\text{ph-ph}} / U_{k,\sigma}.$$

Here, $U_{k,\sigma}$ is the total energy of the coupled mode (\mathbf{k}, σ) per unit volume, $(\frac{\partial U_{k,\sigma}}{\partial t})^{\text{ph-ph}}$ is the rate of change of this energy due to anharmonic decay (or phonon-phonon interaction), and $\tau_{k,\sigma}^{\text{coupled-ph}}$ is the contribution to the lifetime of the coupled mode (\mathbf{k}, σ) due to anharmonic decay.

All changes to the total energy of the coupled mode are due to the response of the system to the total electric field associated with the collective charge oscillation. The loss of energy due to anharmonic decay occurs because the total electric field (of root mean square amplitude \tilde{E}), oscillating at the mode frequency $\omega_{k,\sigma}$, drives the ionic motion. As the ionic motion is damped due to anharmonic decay, energy is dissipated. The rate of energy dissipation per unit volume from the ionic motion due to anharmonic decay is

$$\left(\frac{\partial U_{k,\sigma}}{\partial t}\right)^{\text{ph-ph}} = -\omega_{k,\sigma} \Im(\varepsilon_{k,\omega_{k,\sigma}}^{\text{ph}}) \tilde{E}^2.$$

We do not model the anharmonic decay process itself. We take it to be described by the imaginary part of the ionic dielectric function. This yields

$$1/\tau_{k,\sigma}^{\text{coupled-ph}} = \omega_{k,\sigma} \Im(\varepsilon_{k,\omega_{k,\sigma}}^{\text{ph}}) \tilde{E}^2 / U_{k,\sigma}.$$

Now we can use the same arguments to give the rate of dissipation of energy from the coupled mode (\mathbf{k}, σ) due to the coupling to the carrier gas: the loss of energy due to carrier-carrier interactions occurs because the total electric field (of root mean square amplitude \tilde{E}), oscillating at the mode frequency $\omega_{k,\sigma}$ drives the plasmonic motion. As the motion of the plasma is damped due to carrier-carrier interactions (i.e., Landau damping), energy is dissipated, with the details of the carrier-carrier interactions captured by the imaginary part of the carrier dielectric function:

$$\left(\frac{\partial U_{k,\sigma}}{\partial t}\right)^{c-c} = -\omega_{k,\sigma} \Im(\varepsilon_{k,\omega_{k,\sigma}}^c) \tilde{E}^2.$$

This then gives the rate of decay of the mode (\mathbf{k}, σ) , due to carrier scattering in the second term in the denominator on the r.h.s. of Eq. (16) as

$$\begin{aligned} 1/\tau_{k,\sigma}^{\text{coupled-c}} &= -\left(\frac{\partial U_{k,\sigma}}{\partial t}\right)^{c-c} / U_{k,\sigma} \\ &= \omega_{k,\sigma} \Im(\varepsilon_{k,\omega_{k,\sigma}}^c) \tilde{E}^2 / U_{k,\sigma}. \end{aligned}$$

Note that the ratio $\tilde{E}^2 / U_{k,\sigma}$, which occurs in the energy dissipation rate due to the anharmonic decay, and due to carrier-carrier interaction is a constant for the particular mode (\mathbf{k}, σ) . As the second term in the denominator has already been shown (following Peierls discussion [18]) to be

$$1/\tau_{k,\sigma}^{\text{coupled-c}} = 2F_k^\sigma / v_k \Im(\varepsilon_{k,\omega_{k,\sigma}}^c), \quad (18)$$

this constant equals

$$\tilde{E}^2 / U_{k,\sigma} = \frac{2F_k^\sigma}{v_k \omega_{k,\sigma}}.$$

Consequently, the lifetime of the coupled mode due to anharmonic decay is

$$1/\tau_{k,\sigma}^{\text{coupled-ph}} = 2F_k^\sigma / v_k \Im(\varepsilon_{k,\omega_{k,\sigma}}^{\text{ph}}). \quad (19)$$

Note that the argument depends on the coupling from the collective mode to the ions and to the carriers being through the electric field only (i.e., via the Fröhlich interaction and Coulomb interaction). If a different coupling were present—such as deformation potential coupling—this result would have to be modified.

With Eqs. (18) and (19), the total lifetime of the coupled modes obeys

$$\frac{1}{\tau_{k,\sigma}^{\text{coupled}}} = \frac{2F_k^\sigma}{v_k} \Im(\varepsilon_{k,\omega_{k,\sigma}}^{\text{tot}}), \quad (20)$$

where $\Im(\varepsilon_{k,\omega_{k,\sigma}}^{\text{tot}})$ is the imaginary part of the total dielectric function. This finally gives us the expression for the “coupled mode drag term” G ,

$$G_{k,\sigma} = \frac{2\pi v_k}{\Im(\varepsilon_{k,\omega_{k,\sigma}}^{\text{tot}})} \int_p \delta(E_{p+k} - E_p - \hbar\omega_{k,\sigma}) \times (f_{E_p}^0 - f_{E_{p+k}}^0)(g_{p+k} - g_p). \quad (21)$$

Note that the scattering strength F_k^σ cancels in G . Consequently, G only depends on the mode index σ through the frequency $\omega_{k,\sigma}$, so that we henceforth index G from Eq. (21) with ω rather than σ :

$$G_{k,\omega} = \frac{2\pi v_k}{\Im(\varepsilon_{k,\omega}^{\text{tot}})} \int_p \delta(E_{p+k} - E_p - \hbar\omega) \times (f_{E_p}^0 - f_{E_{p+k}}^0)(g_{p+k} - g_p). \quad (22)$$

G is called a drag term, because the coupled modes are dragged out of equilibrium due their interaction with the carriers. This will be discussed more in Sec. II D 3.

D. Solution of coupled Boltzmann equations

We can now solve the coupled carrier Boltzmann equation and collective mode Boltzmann equation in first order for the nonequilibrium distribution functions g and G . With the first-order field term Eq. (5) and collision term Eq. (8), we get the first-order Boltzmann equation for the carriers

$$-v_p \cdot eE = \int_k \int_{\hbar\omega} W_{k,\omega}^0 \delta(E_{p+k} - E_p - \hbar\omega) \frac{f_{E_{p+k}}^0}{f_{E_p}^0} (N_\omega^0 + 1) \times (g_{p+k} - g_p - G_{k,\omega}), \quad (23)$$

where $G_{k,\omega}$ is determined from Eq. (22), which is also a function of the nonequilibrium carrier distribution functions g .³

1. Iterative solution

We find the solution of the coupled Boltzmann equations by solving Eq. (23) for g and iterating the resulting equation

³Note that Eq. (23) is not defined for all p as the temperature goes to zero and the Fermi-Dirac distribution in the denominator becomes zero for $E_p > E_F$. Consequently, for $E_p > E_F$, $\frac{f_{E_{p+k}}^0}{f_{E_p}^0} (N_\omega^0 + 1)$ has to be replaced with $\frac{1-f_{E_{p+k}}^0}{1-f_{E_p}^0} N_\omega^0$, which holds because the equilibrium distribution functions fulfill an equation of detailed balance.

to self-consistency:

$$\frac{v_p \cdot eE}{g_p^{n+1}} = \int_k \int_{\hbar\omega} W_{k,\omega}^0 \delta(E_{p+k} - E_p - \hbar\omega) \frac{f_{E_{p+k}}^0}{f_{E_p}^0} (N_\omega^0 + 1) \times \left(1 - \frac{g_{p+k}^n}{g_p^n} + \frac{G_{k,\omega}^n}{g_p^n}\right). \quad (24)$$

Here, the n in g^n stands for the n th step in the iteration process. G^n means that G was calculated with $g = g^n$ in Eq. (22). As the g and G depend on the magnitude of the applied field, one usually introduces lifetimes

$$\tau_p = \frac{g_p}{v_p \cdot eE}, \quad (25)$$

which only depend on the direction of the field. We also define a corresponding lifetime

$$T_{k,\omega} = \frac{G_{k,\omega}}{v_k \cdot eE} \quad (26)$$

for the nonequilibrium collective mode. The remaining equation can be expressed as a function of τ_p only, and can be solved iteratively for the latter:

$$\frac{1}{\tau_p^{n+1}} = \int_k \int_{\hbar\omega} W_{k,\omega}^0 \delta(E_{p+k} - E_p - \hbar\omega) \frac{f_{E_{p+k}}^0}{f_{E_p}^0} (N_\omega^0 + 1) \times \left[1 - \frac{\tau_{p+k}^n}{\tau_p^n} \frac{v_{p+k} \cdot E}{v_p \cdot E} + \frac{T_{k,\omega}(\tau_p^n) v_k \cdot E}{\tau_p^n v_p \cdot E}\right]. \quad (27)$$

In Secs. III and V, we will evaluate the equation for semiconductors with spherical parabolic conduction bands. This lets us simplify the expression for τ_p significantly. For details on the evaluation of these and all following integrals for spherical parabolic bands, refer to Appendix C.

2. Initial step and the relaxation time approximation

The better the initial approximation used for τ_p is, the faster the iteration processes converges. We use an approximate solution to the coupled Boltzmann equation as an initial “guess.” For this, we assume parabolic bands. Let us furthermore set $\tau_p^0 = \tau^0$, a constant, for the initial step to the coupled mode solution Eq. (22). As this means that $g_{p+k}^0 - g_p^0 = g_k^0$, we find

$$G_{k,\omega}^0 = g_k^0 \frac{\Im(\varepsilon_{k,\omega}^c)}{\Im(\varepsilon_{k,\omega}^{\text{tot}})}. \quad (28)$$

If we also assume the bands to be spherical, this yields

$$\frac{1}{\tau_p^1} = \int_k \int_{\hbar\omega} W_{k,\omega}^0 \frac{\Im(\varepsilon_{k,\omega}^{\text{ph}})}{\Im(\varepsilon_{k,\omega}^{\text{tot}})} \delta(E_{|p+k|} - E_p - \hbar\omega) \times \frac{f_{E_{|p+k|}}^0}{f_{E_p}^0} (N_\omega^0 + 1) \left[1 - \frac{(p+k) \cdot E}{p \cdot E}\right] \quad (29)$$

for the first step in the iteration. This expression takes the form of the relaxation time approximation, and τ_p^1 can be referred to as the relaxation time solution to the coupled Boltzmann equation.

It is important to understand that our fully self-consistent solution to Eq. (27) goes beyond the relaxation time approximation. We will demonstrate this difference in Sec. VB 3. The nonrelaxation time τ defined in Eq. (25) is sometimes called “effective momentum relaxation time” [12] to stress this point.

Quasielastic approximation. It is clear that the square bracket in Eq. (29) can become negative for certain \mathbf{p} , \mathbf{k} , and ω . If these negative values have enough weight, τ_p^1 itself can become negative, which is nonphysical. If one makes the approximation of quasielastic scattering $|\mathbf{p} + \mathbf{k}| \approx p$ in the square bracket in Eq. (29), however little this might be justified physically, this problem is circumvented, see Appendix C;

$$\frac{1}{\tau_p^1} = \int_{\mathbf{k}} \int_{\hbar\omega} W_{\mathbf{k},\omega}^0 \frac{\Im(\varepsilon_{\mathbf{k},\omega}^{\text{ph}})}{\Im(\varepsilon_{\mathbf{k},\omega}^{\text{tot}})} \delta(E_{|\mathbf{p}+\mathbf{k}|} - E_p - \hbar\omega) \times \frac{f_{E_{|\mathbf{p}+\mathbf{k}|}}^0}{f_{E_p}^0} (N_{\omega}^0 + 1) \left[1 - \frac{\mathbf{k} + \mathbf{p}}{|\mathbf{k} + \mathbf{p}|} \cdot \frac{\mathbf{E}}{p} \right]. \quad (30)$$

In all calculations of the relaxation time τ_p^1 in the results section, Sec. V, we use the quasielastic approximation, Eq. (30).

3. Phonon dissipation weight factor

The scattering rate in Eqs. (29) and (30) is multiplied by the scalar factor

$$C_{\mathbf{k},\omega} = \frac{\Im(\varepsilon_{\mathbf{k},\omega}^{\text{ph}})}{\Im(\varepsilon_{\mathbf{k},\omega}^{\text{tot}})}, \quad (31)$$

which we will call the phonon dissipation weight factor. In a nonpolar material, carrier-coupled mode scattering reduces to carrier-plasmon scattering. This solution has $C_{\mathbf{k},\omega} \equiv 0$, giving an infinite relaxation time, as expected [18]. In an undoped semiconductor with low intrinsic carrier concentration, the coupling between the plasma and the optical phonons is weak, the drag term G vanishes, and only the carrier-LO-phonon scattering need be considered. This solution has $C_{\mathbf{k},\omega} \equiv 1$, reducing Eq. (29) to the usual expression for the relaxation time for carrier-phonon scattering.

We call $C_{\mathbf{k},\omega}$ the phonon dissipation weight factor, because it equals one when the coupled excitations decay infinitely fast, as in the usual approximate treatment of carrier-phonon scattering [34] and zero when the coupled excitations are infinitely long-lived, as in the approximate treatment of carrier-carrier scattering [8]. In general, the intermediate decay rate of the coupled excitations at given wave vectors and frequencies will result in

$$0 \leq C_{\mathbf{k},\omega} \leq 1. \quad (32)$$

This mapping of the decay mechanism onto a scale between 0 and 1 makes the phonon dissipation factor $C_{\mathbf{k},\omega}$ useful in developing an intuition for the character of the coupled modes. Moreover, $C_{\mathbf{k},\omega}$ can be evaluated analytically within the temperature dependent RPA.

We also define an effective scattering rate

$$W_{\mathbf{k},\omega}^{0,\text{eff}} = C_{\mathbf{k},\omega} W_{\mathbf{k},\omega}^0, \quad (33)$$

which will be illustrated in Sec. III B. Through the phonon dissipation weight factor, the effective scattering rate is only large when a carrier scatters strongly with a coupled mode such

that carrier momentum is lost through anharmonic decay, not when the carrier just scatters strongly with a coupled mode. Therefore the effective scattering rate is a better measure of momentum relaxation than the scattering rate alone.

E. Drift mobility in two or three dimensions

When the self-consistent effective momentum relaxation time, the $n \rightarrow \infty$ solution of Eq. (27), depends only on the magnitude of the wave vector, $\tau_p = \tau_p$, we can express the drift mobility as

$$\mu = \frac{e}{m^*} \frac{\int_0^\infty dp p^{d+1} f_{E_p}^0 (1 - f_{E_p}^0) \tau_p}{\int_0^\infty dp p^{d+1} f_{E_p}^0 (1 - f_{E_p}^0)}, \quad (34)$$

where $d = 2$ or 3 , for the two- or three-dimensional case, respectively. Here, e is the electron charge and m^* is the effective mass.

III. COUPLED COLLECTIVE MODE SCATTERING IN BULK POLAR SEMICONDUCTORS

The formalism developed in Sec. II is applicable to polar semiconductors in general. The level of approximation manifests itself in the expressions used for the dielectric functions. In principle, one could use expressions for the carrier and lattice dielectric functions extracted from electron and phonon band-structure calculations. In practice, we expect our assumptions to work best, and to be most consistent with each other, for screened electron-LO-phonon scattering in semiconductors with a parabolic conduction band. We consider n -type semiconductors, because conduction bands are usually better described with parabolic approximations than valence bands [35]. We take the doping concentrations to be low enough that higher bands are not significantly occupied and that the conduction band can be described as parabolic. Consequently, we can use model carrier dielectric functions for parabolic bands [15,36]. Moreover, the wave vectors at the bottom of the conduction band relevant for intravalley scattering will be small on the scale of the Brillouin zone, so that the assumption that the scattering strength $F_{\mathbf{k}}^\sigma$ only depends on the transferred wave vector and not the initial or final wave vector should be good. This also justifies the use of the long-wavelength limit of the lattice dielectric function. All these approximations are common for the calculations of electron-LO-phonon scattering in bulk semiconductors, see, e.g., Ref. [34].⁴ Our phenomenological account of the lifetime of the coupled plasmon-LO-phonon modes is new, but nonetheless consistent with previous treatments of electron-LO-phonon scattering and electron-electron scattering in the appropriate limits (see Appendix A and Refs. [7,17,34,37]).

In this section, we demonstrate the qualitative effects of screening on carrier-LO-phonon scattering, for simple model

⁴This can be seen in Eq. (5) of Ref. [34], where the $W_{E/A}(\mathbf{k}, \mathbf{k}')$ (which are not identical to our $W_{\mathbf{k}}^0$) only depend on \mathbf{k} and \mathbf{k}' explicitly due to the energy conservation delta function.

dielectric functions. This allows us to get insight into the basic concepts of coupled collective mode scattering, while also being directly applicable to screened LO-phonon scattering in bulk semiconductors such as GaAs, which can be well described by carriers in a single parabolic conduction band interacting with a single LO mode.

All plots of scattering matrix elements in this section are for GaAs, the prototypical polar semiconductor. In Sec. III C, we explore how the screened LO-phonon limited mobility depends on material parameters, specifically the carrier effective mass, optical phonon frequencies and dielectric constants, by calculating mobilities for a selection of polar semiconductors.

A. Dielectric functions

Varga [10] noted that within the RPA, the lattice and the carrier susceptibilities can simply be added to yield the total dielectric function:

$$\epsilon_{\mathbf{k},\omega}^{\text{tot}} = \epsilon_{\mathbf{k},\omega}^{\text{ph}} + \epsilon_{\mathbf{k},\omega}^c - \epsilon^\infty. \quad (35)$$

In our notation, both ϵ^{ph} and ϵ^c include the dielectric response of the valence electrons, ϵ^∞ , so that $\lim_{\omega \rightarrow \infty} \epsilon^c = \epsilon^\infty$ and $\lim_{\omega \rightarrow 0} \epsilon^{\text{ph}} = \epsilon^\infty$. We show in Appendix A how various approximations for the dielectric function recover different limiting cases of carrier scattering that have been treated by previous authors.

1. Carrier dielectric function ϵ^c for nonzero temperatures

We employ a Lindhard-type or RPA carrier dielectric function [15,30], but for nonzero temperatures [36]. The nonzero temperature dielectric functions allow us to consider any point of the sliding scale between the classical and the extreme quantum limit. The real part of the temperature dependent RPA dielectric functions has to be evaluated numerically [36], but its imaginary part can be expressed analytically. See, for example, Sec. 5.5 of Ref. [38]. We assume that there is only one spherical, parabolic conduction band populated, and the equations for the effective momentum relaxation rates in Appendix C make use of the simplifications which follow. For the dielectric functions, this means that they only depend on the magnitude and not on the direction of the wave vector.

2. Lattice dielectric function ϵ^{ph}

We use the model lattice dielectric function [35] Eq. (1) which fulfills the Lyddane-Sachs-Teller [16] relation $\frac{\epsilon_0}{\epsilon^\infty} = \frac{\omega_{\text{LO}}^2}{\omega_{\text{TO}}^2}$. We list the parameters in Eq. (1) for the semiconductors investigated in Sec. III C in Table I. The assumption of constant optical phonon frequencies is well justified on the length scale of an inverse Fermi wave vector relevant for mobility calculations. Even for very high doping at $n = 5 \times 10^{19} \text{ cm}^{-3}$, the Fermi wave vector $k_F = 1.14 \times 10^7 \text{ cm}^{-1}$ is still about a factor of five smaller than $\frac{\pi}{a} = 5.56 \times 10^7 \text{ cm}^{-1}$, the width of the Brillouin zone in [100] direction in GaAs. We are in the long-wavelength limit for phonons, but not for plasmons.

B. Scattering rates

The scattering rate is affected by temperature and anharmonic damping in three different ways. Firstly, the modes

TABLE I. Material parameters for coupled collective mode scattering. Parameters from Ref. [35] unless indicated otherwise. For simplicity, we assume that these parameters do not change with temperature or carrier concentration.

	GaAs	InAs ^a	InP	InSb ^b	ZnSe	PbTe ^c	ZnS ^d
$\hbar\omega_{\text{LO}}(\text{meV})$	36.14	30.2	43.1	23.6	31.9	13.65	36.9
$\hbar\omega_{\text{TO}}(\text{meV})$	33.25	27.1	38.1	22.2	26.2	3.97	28.40
ϵ^∞	11.1	11.8	9.52	15.7	5.9	32.8	4.9
m^*/m_e	0.067	0.026	0.073	0.014	0.134	0.038	0.34
$\gamma/\omega_{\text{TO}}$	0.007	0.01	0.01	0.016	0.01	0.65	0.01
$n_C(10^{17} \text{ cm}^{-3})$	7.04	2.02	9.36	0.89	5.82	1.68	16.5

^aExperimental value for γ is an upper limit.

^bEffective mass from Ref. [40].

^cEffective mass from Ref. [11], other parameters from Ref. [41]. PbTe bands are highly anisotropic and anisotropic, but have been approximately described with a single effective mass before [11].

^dParameters from Ref. [40], set $\gamma = \gamma_{\text{ZnSe}}$ due to lack of γ_{ZnS} in the literature.

start to blur abruptly as soon as they move into the single pair excitation regime. This can be seen in the plot of $\Im m(\frac{1}{\epsilon_{\text{tot}}})$ [Fig. 1(a)], where the electronic dielectric function is the $T = 0$ RPA dielectric function, and the lattice dielectric function is the $\gamma \rightarrow 0$ limit of Eq. (1). This shows that the excitation of quasi-electron-hole pairs is captured by the RPA dielectric

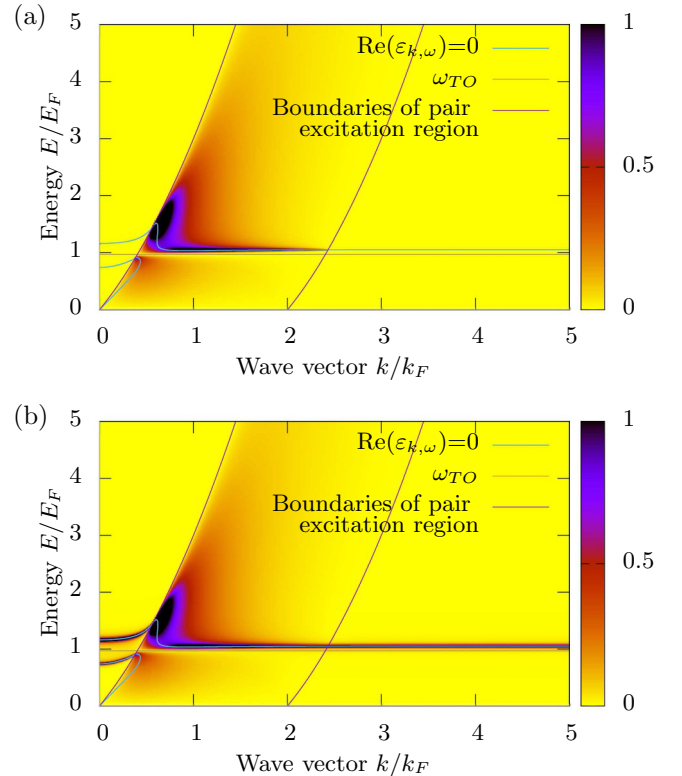


FIG. 1. $\Im m(-\frac{1}{\epsilon_{\text{tot}}})$ in GaAs at $T = 0$ and $n = 5 \times 10^{17} \text{ cm}^{-3}$ with an anharmonic optical phonon damping rate (a) $\gamma = 0$, and (b) $\gamma = 0.007\omega_{\text{TO}}$, as a function of wave vector k and energy $E = \hbar\omega$.

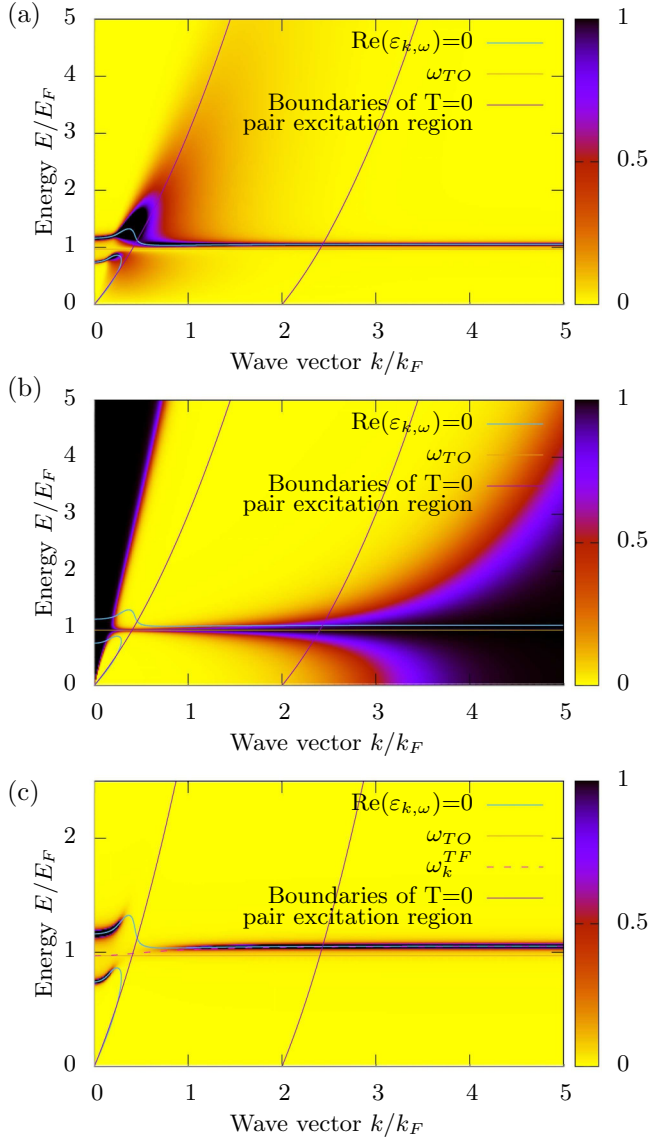


FIG. 2. (a) $\text{Im}(-\frac{\epsilon_{\text{tot}}^\infty}{\epsilon_{k,\omega}}) \propto W_{k,\omega}^0/\nu_k$, the scattering rate Eq. (10), (b) phonon dissipation weight factor $C_{k,\omega}$, Eq. (31), and (c) $C_{k,\omega} \text{Im}(-\frac{\epsilon_{\text{tot}}^\infty}{\epsilon_{k,\omega}}) \propto W_{k,\omega}^{0,\text{eff}}/\nu_k$, the effective scattering rate Eq. (33), for GaAs at $n = 5 \times 10^{17} \text{ cm}^{-3}$ and $T = 300 \text{ K}$ as a function of wave vector k and energy $E = \hbar\omega$.

function, as expected. Secondly, the damping rate in the lattice dielectric function broadens the LO-phonon peak from a delta peak to a Lorentzian, and also has an effect on the width of the coupled peaks before they reach the single pair excitation regime, see Fig. 1(b). Thirdly, the temperature dependence in the electronic part of the dielectric function again broadens both coupled peaks. Moreover, it causes the boundaries of the single pair excitation limit to blur. For an example, compare Fig. 1(b) with Fig. 2(a), which shows $\text{Im}(\frac{1}{\epsilon_{\text{tot}}})$ for $T > 0$. This blurring occurs, because of the thermal excitation of quasielectrons and quasiholes from the Fermi sea. In the classical limit, this contribution to the damping of the modes is referred to as Landau damping [39].

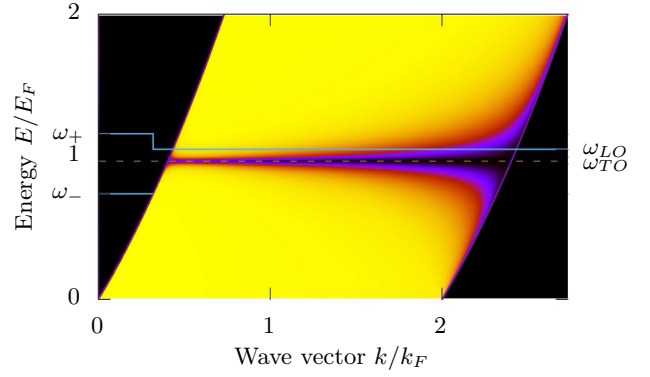


FIG. 3. Phonon dissipation factor $C_{k,\omega}$, Eq. (31), for GaAs at $T = 0$, $n = 5 \times 10^{17} \text{ cm}^{-3}$, as a function of wave vector k and energy $E = \hbar\omega$. The legend for the color plot is the same as in Fig. 2. Also shown are the coupled modes in the approximation by Fischetti *et al.* [13], Sec. A3.

1. Phonon dissipation weight

The phonon dissipation weight factor Eq. (31) [Fig. 2(b)] introduced in Sec. IID 3, which provides a measure of the decay mechanism of the coupled modes, can be evaluated analytically with the carrier dielectric function discussed in Sec. III A 1 and the lattice dielectric function Eq. (1). We find the phonon dissipation weight factor

$$\tilde{C}_{K,\Omega} = \left\{ 1 + \frac{2[(\Omega_{\text{TO}}^2 - \Omega^2)^2 + \Omega^2 \Gamma^2]}{E_F \beta k_F a_0^* (\Omega_{\text{LO}}^2 - \Omega_{\text{TO}}^2) \Gamma \Omega K^3} \times \ln \left[\frac{1 + e^{\beta \nu - .5 E_F \beta (\Omega/K - K)^2}}{1 + e^{\beta \nu - .5 E_F \beta (\Omega/K + K)^2}} \right] \right\}^{-1}, \quad (36)$$

where the capital letters all stand for dimensionless quantities, defined by the same lower case letter scaled by the Fermi wave vector or energy, $K = k/k_F$, $\Omega = \hbar\omega/E_F$, $\Omega_{\text{LO/TO}} = \hbar\omega_{\text{LO/TO}}/E_F$, $\Gamma = \hbar\gamma/E_F$, and $a_0^* = \frac{\epsilon^\infty \hbar^2}{m^* e^2}$ is the effective Bohr radius with the effective mass m^* . Note that the phonon dissipation factor only makes sense when the damping of the optical phonons is finite, i.e., $\gamma > 0$.

In the zero-temperature limit, $\text{Im}(\epsilon^c)$ vanishes outside the single-pair excitation region. Consequently, $C_{k,\omega}^{T=0} = 1$ everywhere except the single pair excitation region, see Fig. 3.

2. Effective scattering rate

The effective scattering rate Eq. (33) governs the momentum relaxation time τ_p^1 from Eq. (29). As plotted in Fig. 2(c), it is the product of the scattering rate [Fig. 2(a)] and the phonon dissipation weight factor [Fig. 2(b)]. As the imaginary part of the carrier dielectric function is an odd function of K , $\tilde{C}_{K,\Omega} \rightarrow 1$ as $K \rightarrow 0$, see Fig. 2(b). This ensures that our effective scattering rate and the scattering rate are equal in the long-wavelength limit. We see that, as not only the scattering rate, but also the dissipation mechanism is important, the effective scattering rate is only significant close to the zeros of the real part of the dielectric function.

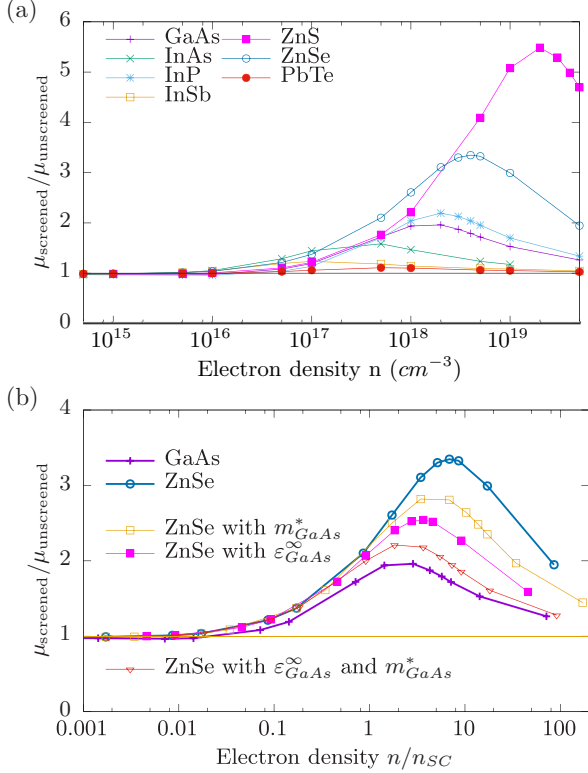


FIG. 4. Ratio $\frac{\mu_{\text{screened}}}{\mu_{\text{unscreened}}}$ at $T = 300$ K (a) for n -type GaAs, InAs, InP, InSb, ZnSe, PbTe, and ZnS depending on electron density (b) for n -type GaAs, ZnSe, and hypothetical materials with mixed GaAs and ZnSe parameters, depending on electron density normalized by their respective characteristic density n_C .

C. Screening of LO-phonon scattering depending on material parameters

Whether explicit treatment of coupled collective mode scattering is important for the carrier mobility in a material depends on two factors. Firstly, coupled collective mode scattering has to differ significantly from LO-phonon scattering for a certain density. Secondly, polar scattering mechanisms have to be an important scattering mechanism at that density. This depends on the other relevant scattering mechanisms in the material.

In this section, we address the first factor for some polar semiconductors similar to GaAs. We also describe them with a single spherical parabolic conduction band, and compare the mobility limited by coupled collective mode scattering (“ μ_{screened} ”) to the mobility due to LO-phonon scattering (“ $\mu_{\text{unscreened}}$ ”). Appendix C describes the evaluation of the momentum relaxation time in detail, where Eq. (C14) is the expression for the momentum relaxation time in the screened case. For the unscreened case, we have to set $T_{K,\Omega} = 0$ and $\epsilon^{\text{tot}} \approx \epsilon^{\text{ph}}$ in the scattering rate Eq. (10), which enter into Eq. (C14). The mobilities are calculated from Eq. (34). The parameters used for these calculations are given in Table I, and the ratio of the screened to the unscreened LO-phonon mobility $\frac{\mu_{\text{screened}}}{\mu_{\text{unscreened}}}$ is plotted for some n -type materials at room temperature in Fig. 4(a).

In the long-wavelength limit, the coupling between LO-phonons and plasmons is strongest when the plasma frequency

and the LO-phonon frequency are similar (see Fig. 17 in Appendix A) or

$$n \approx n_C = \frac{\omega_{\text{LO}}^2 m^* \epsilon^\infty}{4\pi e^2}. \quad (37)$$

We see that $\frac{\mu_{\text{screened}}}{\mu_{\text{unscreened}}}$ is slightly smaller than one for low carrier densities (“antiscreening”), and larger than one (“screening”) for high carrier densities across all materials. The ratio $\frac{\mu_{\text{screened}}}{\mu_{\text{unscreened}}}$ has a broad peak around $n = n_C$, and decreases towards one again for larger n .

The curve for InP, which has very similar m^* , 14% lower ϵ^∞ and higher optical phonon frequencies than GaAs, is very similar to the GaAs curve. InAs, which has a much smaller m^* than GaAs or InP, similar ϵ^∞ to GaAs and smaller optical phonon frequencies, has smaller maximal $\frac{\mu_{\text{screened}}}{\mu_{\text{unscreened}}}$. InSb, which is even lighter, and has higher ϵ^∞ , has even lower $\frac{\mu_{\text{screened}}}{\mu_{\text{unscreened}}}$. PbTe has the smallest maximal $\frac{\mu_{\text{screened}}}{\mu_{\text{unscreened}}}$ of all considered materials. It has quite a low effective mass, and the highest ϵ^∞ of all considered materials. Moreover, its optical phonon frequencies are very small, with ω_{TO} only a fraction of ω_{LO} .

We see much larger $\frac{\mu_{\text{screened}}}{\mu_{\text{unscreened}}}$ in ZnSe, which has roughly twice the GaAs effective mass and half its ϵ^∞ , and whose optical phonon frequencies are similar to InAs. ZnS, which has even higher m^* and lower ϵ^∞ than ZnSe, shows the largest $\frac{\mu_{\text{screened}}}{\mu_{\text{unscreened}}}$ of the investigated materials.

To investigate how $\frac{\mu_{\text{screened}}}{\mu_{\text{unscreened}}}$ depends on the parameters, we consider hypothetical materials that have (1) ZnSe parameters, but a GaAs effective mass, (2) ZnSe parameters, but a GaAs ϵ^∞ , (3) ZnSe parameters, but GaAs ϵ^∞ and m^* . When we change ϵ^∞ , we leave ω_{LO} and ω_{TO} constant, but adjust ϵ^0 to satisfy the Lyddane-Sachs-Teller relation.

Figure 4(b) shows that $\frac{\mu_{\text{screened}}}{\mu_{\text{unscreened}}}$ grows with increasing m^* and falls with increasing ϵ^∞ . Changing the ZnSe effective mass and ϵ^∞ to their GaAs value results in a $\frac{\mu_{\text{screened}}}{\mu_{\text{unscreened}}}$, which is very similar to the GaAs curve. Extrapolating from the comparison between GaAs and ZnSe, and the trend observed in Fig. 4(a), we expect the relative difference between screened and unscreened LO-phonon mobility to be largest in materials with large effective mass and low high-frequency dielectric constant. We can explain this trend qualitatively. The Thomas-Fermi wave vector k_{TF} is proportional to the effective mass, and the static free carrier susceptibility proportional to k_{TF} for small k . That means that the free carrier susceptibility will be the more important compared to the valence band susceptibility ϵ^∞ if the latter is small, or if m^* is large. In materials that are very strongly polar, like PbTe, ϵ^0 is much larger than ϵ^∞ , and the free carrier susceptibility plays an even smaller role.

IV. SCREENED INTERFACE POLAR PHONON SCATTERING

The formalism developed in Sec. II can be applied to semiconductor heterostructures directly. One only has to find the appropriate dielectric functions for these composite structures. Maslov [20] did this to describe the Coulomb drag between a 2D electron gas (2DEG) in interaction with a 3D electron gas. His approach has been applied to coulomb drag in various heterostructures, e.g., Refs. [42,43], and also to

remote phonon scattering, the interaction of a 2DEG with the surrounding optical phonons [44]. We will refer to this as screened interface phonon scattering.

Following Maslov [20], we use the fluctuation-dissipation theorem to describe interface scattering with the scattering rate⁵

$$W_{k,\omega}^0 \propto \int dz_1 \int dz_2 \psi_n^2(z_1) \psi_n^2(z_2) \Im(\varphi_{k,\omega}(z_1, z_2)), \quad (38)$$

where φ is the electrostatic potential at point z_1 introduced by a point charge at z_2 in the interface. \mathbf{k} is the wave-vector component parallel to the interface and ω the frequency of the relevant excitation. ψ_n is the transverse wave function of the carriers in the n th subband inside the interface.

If we take the interface to be infinitely thin and situated at $z = 0$, $\psi_n(z) \propto \delta(z)$, so that

$$W_{k,\omega}^0 \propto \Im(\varphi_{k,\omega}(z_1 = 0, z_2 = 0)), \quad (39)$$

and we only have to determine the electrostatic potential $\varphi_{k,\omega}(0,0)$ at $z_1 = 0$ due to a point charge at $z_2 = 0$. We will drop the argument $z_2 = 0$ on φ in the subsequent discussion.

A. Solution of the Poisson equation in a heterostructure of anisotropic dielectrics

As Maslov [20] discusses a case with isotropic dielectrics, we show the solution to the Poisson equation for a heterostructure of anisotropic, dispersive media, and a sheet charge density in an interface at $z = 0$. Away from the interfaces, the potential φ fulfills the Laplace equation

$$-\sum_{i,j} \varepsilon^{ij} \partial^i \partial^j \varphi = 0 \quad (40)$$

with a dielectric tensor ε^{ij} , which is constant or sufficiently slowly varying in space. If we assume that the interface is aligned with one of the principal axes in the crystal, $\varepsilon^{ij} = \delta^{ij} \varepsilon^{ii}$ becomes diagonal. We also assume that the two principal axes parallel to the interface have the same dielectric constant, $\varepsilon^{xx} = \varepsilon^{yy}$. If $\varphi_{k,\omega}(z)$ is the Fourier transform of $\varphi(x, y, z, t)$ in the x and y coordinates, and in time, the Laplace equation becomes

$$\left(\frac{\partial^2}{\partial z^2} - \frac{\varepsilon^{xx}}{\varepsilon^{zz}} |\mathbf{k}|^2 \right) \varphi_{k,\omega}(z) = 0. \quad (41)$$

We can introduce the scaled wave vector K with

$$K_{k,\omega} = k \sqrt{\frac{\varepsilon^{xx}}{\varepsilon^{zz}}} \quad (42)$$

in order to write the anisotropic Laplace equation the same way as the isotropic one:

$$\left(\frac{\partial^2}{\partial z^2} - K^2 \right) \varphi_{k,\omega}(z) = 0. \quad (43)$$

⁵Note that Maslov's notation differs from ours. In particular, our symbol W and his do not have the same meaning. Our $\varphi_{k,\omega}(z_1, z_2)$ corresponds to his $D(\omega, \mathbf{q}, z_1, z_2)$.

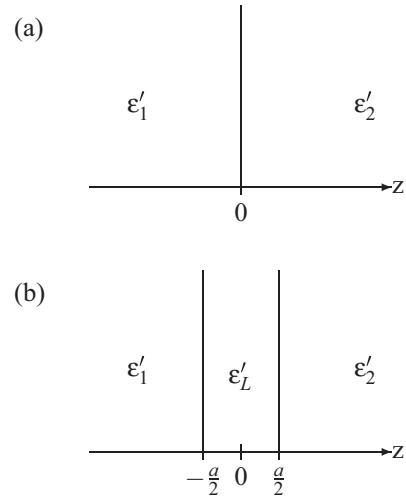


FIG. 5. Interface layer with the dielectric function ε'_L between two dielectrics with the dielectric functions ε'_1 and ε'_2 on the left and right, respectively. (a) Assuming the interface is infinitely thin. (b) The interface has a finite thickness a .

In general, all dielectric functions, and hence K , are complex. We choose the root in Eq. (42), to lie in the right half-plane, $\Re(K) > 0$. Hence we know that the term $\propto e^{-Kz}$ in the solution to the differential equation of second-order equation (43),

$$\varphi_{k,\omega}(z) = \alpha e^{-Kz} + \beta e^{Kz}, \quad (44)$$

corresponds to an exponentially decreasing oscillatory term, whereas the term $\propto e^{Kz}$ corresponds to an exponentially growing one. Equation (44) requires two boundary conditions to determine the complex coefficients α and β . For convenience, we introduce the quantity

$$\varepsilon'_{\omega} \equiv \varepsilon_{\omega}^{zz} \sqrt{\frac{\varepsilon_{\omega}^{xx}}{\varepsilon_{\omega}^{zz}}}, \quad (45)$$

an effective scalar dielectric function.⁶

1. Boundary conditions

In a system with a series of homogeneous dielectrics changing along the z axis, between interfaces $z = z_n$ (Fig. 5), there are three kinds of boundary conditions.

(1) The potential on the edges of the relevant domain needs to be known. We use the requirement $\lim_{z \rightarrow \pm\infty} \varphi_{k,\omega}(z) = 0$ that the potential vanishes far away from the interface.

(2) The potential has to be continuous at the interfaces:

$$\lim_{\delta \rightarrow 0} \varphi_{k,\omega}(z_n - \delta) = \lim_{\delta \rightarrow 0} \varphi_{k,\omega}(z_n + \delta). \quad (46)$$

(3) The component of the dielectric displacement D^z perpendicular to the interface on either side of the interface has to differ by the surface charge $\sigma_{k,\omega}$:

$$\lim_{\delta \rightarrow 0} D_{k,\omega}^z(z_n + \delta) - \lim_{\delta \rightarrow 0} D_{k,\omega}^z(z_n - \delta) = 4\pi \sigma_{k,\omega}. \quad (47)$$

⁶Again, we take the root in the right half-plane.

With the dielectric displacement D^z defined as

$$D_{k,\omega}^z = \varepsilon^{zz} E_{k,\omega}^z = -\varepsilon^{zz} \frac{\partial}{\partial z} \varphi_{k,\omega}(z), \quad (48)$$

this can be written as

$$\varepsilon_{n+1}^{zz} \lim_{\delta \rightarrow 0} \frac{\partial}{\partial z} \varphi_{k,\omega}(z_n + \delta) - \varepsilon_n^{zz} \lim_{\delta \rightarrow 0} \frac{\partial}{\partial z} \varphi_{k,\omega}(z_n - \delta) = -4\pi \sigma_{k,\omega}, \quad (49)$$

where ε_n is the dielectric to the left of the interface at z_n and ε_{n+1} the dielectric to the right of the interface at z_n . Both these dielectric functions can depend on frequency, the frequency index has been suppressed in Eq. (49) for brevity. For a system with n interfaces, and $n + 1$ different layers, this will yield $2n + 2$ equations for the $2(n + 1)$ variables α_n and β_n .

B. Effective scalar dielectric function $\varepsilon^{\text{interface}}$ for the heterostructure

Imagine a 2D test sheet charge density at $z = 0$, which is constant as a function of wave vector and frequency, $\sigma_{k,\omega} = \sigma$, surrounded by a uniform medium with the dielectric function $\varepsilon_{\omega}^{\text{uniform}}$. This gives rise to a potential

$$\varphi_{k,\omega}^{\text{uniform}}(z = 0) = \frac{2\pi\sigma}{k\varepsilon_{\omega}^{\text{uniform}}} \quad (50)$$

at $z = 0$. We define an effective dielectric constant $\varepsilon_{k,\omega}^{\text{interface}}$ due to a test charge density σ at $z = 0$ in the composite system as

$$\varepsilon_{k,\omega}^{\text{interface}} \equiv \frac{2\pi\sigma}{k\varphi_{k,\omega}^{\text{interface}}(z = 0)} \quad (51)$$

so that Eq. (50) for the uniform background holds for the case with the interface. With Eq. (51), we can express the scattering rate in terms of the imaginary part of the inverse dielectric function:

$$W_{k,\omega}^0 = \frac{2\nu_k}{\hbar} \text{Im} \left(\frac{-1}{\varepsilon_{k,\omega}^{\text{interface}}} \right). \quad (52)$$

For the example in Fig. 5(a), an interface between two different dielectrics, we get

$$\varepsilon^{\text{interface 1a}} = \frac{1}{2}(\varepsilon'_1 + \varepsilon'_2). \quad (53)$$

We can retrieve Hess and Vogl's [19] case of remote polar phonon modes at the interface between a nonpolar semiconductor and an oxide if we set $\varepsilon'_1 = \varepsilon_S^\infty$ and $\varepsilon'_2 = \varepsilon_{ox}$ to Eq. (1) with $\gamma = 0$.

For the example in Fig. 5(b), a thin layer with dielectric ε'_L between two different dielectrics, the same procedure yields

$$\varepsilon^{\text{interface 1b}} = \varepsilon'_L \frac{B - A}{(1 + A)(1 + B)} \quad \text{with } A = \frac{\varepsilon'_L - \varepsilon'_1}{\varepsilon'_L + \varepsilon'_1} e^{-K_L a},$$

$$B = \frac{\varepsilon'_L + \varepsilon'_2}{\varepsilon'_L - \varepsilon'_2} e^{K_L a}. \quad (54)$$

In the examples, we indexed the effective dielectric functions ε' , Eq. (45) and the scaled wave vector K , Eq. (42) with the indices 1 and 2 for the left and right sides of the interface and with an "L" for layer in the case where there is a small interface layer of thickness a [see Fig. 5(b)].

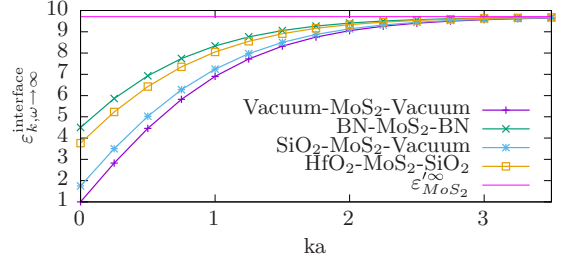


FIG. 6. High-frequency interface dielectric function $\varepsilon_{k,\omega \rightarrow \infty}^{\text{interface}}$ as a function of the wave vector times the interface layer thickness a [see Eq. (54)] for different structures discussed in Sec. V. The lines are marked with the materials which make up the heterostructure described in Fig. 5(b), in the order “left dielectric”-“interface layer material”-“right dielectric”. In this plot, the interface layer is always MoS₂, with a thickness of $a = 6.145 \text{ \AA}$, as discussed in Sec. V A.

The high-frequency limit of Eq. (54) is shown as a function of layer thickness in Fig. 6. It is equal to Eq. (53) for zero wave vector k , and goes towards the high-frequency dielectric function of the layer material, ε_L^∞ as $k \rightarrow \infty$.

C. Dielectric response of carriers: Screening of polar interface modes

As we assume that all free carriers are localized in the plane at $z = 0$, we can use purely two-dimensional expressions for the dielectric response of the carrier gas. Stern gave the expression for the dielectric function of a two-dimensional electron gas surrounded by a homogeneous dielectric medium [21]:

$$\varepsilon_{k,\omega}^c = \varepsilon^b + 2\pi |k| \chi_{k,\omega}, \quad (55)$$

where $\chi_{k,\omega}$ is the susceptibility of the two-dimensional electron gas in the RPA, and ε^b is the high-frequency dielectric constant of the background medium.⁷ Following Maslov [20], we use Stern's dielectric function, replacing the dielectric constant for the homogeneous surrounding medium with the dielectric function of our composite structure, $\varepsilon^{\text{interface}}$. This yields the total dielectric function (phonon and plasmon response) of the composite structure

$$\varepsilon_{k,\omega}^{\text{tot}} = \varepsilon_{k,\omega}^{\text{interface}} + 2\pi |k| \chi_{k,\omega} = \varepsilon_{k,\omega}^{\text{interface}} + \varepsilon_{k,\omega}^c - \varepsilon^b. \quad (56)$$

This expression is formally identical to the expression for the total dielectric function in the bulk case, Eq. (35), with $\varepsilon^{\text{interface}}$, the dielectric response of a polar composite structure replacing ε^{ph} , the dielectric function of a polar bulk material. As such, we can directly apply the formalism developed in Sec. II for bulk materials to composite structures, using

$$W_{k,\omega}^0 = \frac{2\nu_k}{\hbar} \text{Im} \left(\frac{-1}{\varepsilon_{k,\omega}^{\text{tot}}} \right). \quad (57)$$

As more different materials are involved in composite structures, the calculations become more complex than in the

⁷We neglect retardation effects which are present in Stern's expression.

bulk case. Even when neglecting the dielectric response of the carriers, the multiple optical modes from different constituents of the composite structures will couple. To avoid confusion with the coupled collective phonon-plasmon modes in the simpler bulk case, we will call these coupled optical modes unscreened interface modes. When we take the carrier response into account, we obtain screened interface modes. In general, we treat this screening dynamically. As static screening is a common approximation, we also consider this limit.

Stern gives an analytical expression for the susceptibility in the zero temperature limit [21]. There are also analytical expressions for the high-temperature limit [45]. Maldague gives a semianalytical formula for the temperature dependence of the static susceptibility [46], which is commonly used for capturing static screening.

We evaluate the RPA susceptibility explicitly, with the full temperature, wave-vector, and frequency dependence. Only by including the full frequency dependence can we describe dynamic screening. While the imaginary part of the susceptibility can be expressed through Fermi-Dirac integrals the real part of the susceptibility requires numerical evaluation [43].

V. SCREENED INTERFACE PHONON SCATTERING IN POLAR MoS_2 HETEROSTRUCTURES

We calculate the carrier mobility due to interface phonon-plasmon scattering for MoS_2 -sandwiches, that is, for a single layer of MoS_2 between dielectric 1 on the one side and dielectric 2 on the other side [Fig. 5(b)]. We first calculate the effective momentum relaxation time from Eq. (27). We discuss how this expression is calculated in detail in Appendix D, yielding Eq. (D7) for the fully self-consistent effective momentum relaxation time. We discuss the treatment of screening in detail in Sec. VB 2. In the second step, we then calculate the carrier mobilities from the momentum relaxation times using Eq. (34).

In order to assess the mobility that could be achieved in a device that is not dominated by charged impurity scattering, we include acoustic deformation potential scattering, piezoelectric scattering and optical deformation potential scattering in the calculation of the total mobility, using the parameters calculated by Kaasbjerg *et al.* [26,29].

In Appendix E, we describe how to calculate the momentum relaxation times due to acoustic and optical deformation potential scattering and piezoelectric scattering [25,26,29]. Like Kaasbjerg *et al.* [29], but unlike Ma and Jena [25], we do not think longitudinal optical phonon scattering in the layer of MoS_2 itself contributes significantly to the scattering. See Appendix E for details.

We then calculate a “total” momentum relaxation time τ_{tot} due to these scattering processes, and screened interface phonon scattering from

$$\tau_{\text{tot}} = \frac{1}{\sum_i \frac{1}{\tau_i}}, \quad (58)$$

where the sum is over the different scattering processes above. We put quotes around total here, because in realistic structures, the mobility is often dominated by charged impurity scattering caused by a large number of defects [27,28], which we do not

include here. The corresponding “total” mobility μ_{tot} due to acoustic and optical deformation potential scattering, piezoelectric scattering and screened interface phonon scattering is calculated by substituting τ_{tot} in Eq. (34).

A. Modelling of materials

1. Oxides

We use a phenomenological model for the ionic dielectric response of the different dielectric layers, using data from infrared and Raman spectroscopy. All parameters used can be found in Table II. We account for two damped optical phonon modes:

$$\varepsilon_\omega = \varepsilon^\infty + \frac{(\varepsilon^0 - \varepsilon^i)\omega_{\text{TO},1}^2}{\omega_{\text{TO},1}^2 - \omega^2 + i\omega\gamma_1} + \frac{(\varepsilon^i - \varepsilon^\infty)\omega_{\text{TO},2}^2}{\omega_{\text{TO},2}^2 - \omega^2 + i\omega\gamma_2}. \quad (59)$$

A dielectric response of this kind can be parametrized in many equivalent ways (compare Ref. [47] with Eq. (59))—we use a parametrization of the scattering strength in terms of an intermediate dielectric constant ε^i , as Fischetti *et al.* [13], but with nonzero damping rates for the optical modes. Here, ε^0 is the static and ε^∞ the high-frequency dielectric constant, $\omega_{\text{TO},1}$ is the lower frequency transverse optical mode frequency and γ_1 the corresponding damping rate, and $\omega_{\text{TO},2}$ is the lower frequency transverse optical mode frequency and γ_2 the corresponding damping rate. Setting $\varepsilon^i = \varepsilon^0$ or $\varepsilon^i = \varepsilon^\infty$ recovers Eq. (1), a dielectric response with just one optical resonance.

Some of the polar materials discussed here have strongly anisotropic dielectric functions [47,48]. These are layered materials, where the in-plane dielectric function differs strongly from the out-of-plane dielectric function. As the anisotropic structures discussed are stacks of monolayers, the crystal axes of the various materials align with the interfaces between the layer (x - y plane) and the axes perpendicular to it (z axis, see Fig. 5). Consequently, the dielectric function parallel to the hexagonal c axis, ε^\parallel as used by Refs. [47,48], is equal to ε^{zz} , and the dielectric function perpendicular to the c axis, ε^\perp is the same as ε^{xx} .

2. Channel material

Hexagonal molybdenite in its bulk form has been long known and characterized (see [48] for its crystal structure). Bulk MoS_2 (2H) consists of weakly bonded layers with a

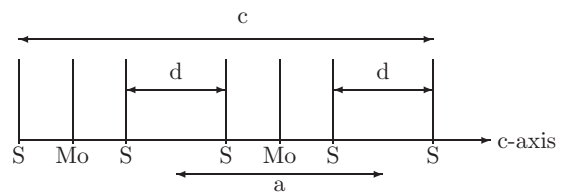


FIG. 7. Projection of the MoS_2 (2H) primitive unit cell onto the c axis, to scale. Lines perpendicular to the c -axis mark the planes in which the marked atoms sit. The length of the unit cell is $c = 12.29 \text{ \AA}$, the interatomic distance is $d = 2.96 \text{ \AA}$ [48]. The size of a unit cell of a monolayer $a = c/2 = 6.145 \text{ \AA}$.

TABLE II. Material parameters for model dielectric functions.

Material		ϵ^∞	ϵ^i	ϵ^0	$\omega_{\text{TO},1}$ (meV)	γ_1 (meV)	$\omega_{\text{TO},2}$ (meV)	γ_2 (meV)
MoS ₂ ^a	ϵ^{xx}	15.2		15.4	47.61	0.12		
	ϵ^{zz}	6.2		6.23	58.27	0.29		
BN ^b	ϵ^{xx}	4.95	6.82	7.04	95.10	4.34	169.49	3.60
	ϵ^{zz}	4.10	4.56	5.09	97.08	0.99	187.22	9.92
SiO ₂ ^c	$\epsilon^{xx} = \epsilon^{zz}$	2.5	3.05	3.9	55.6	0.56	138.1	1.38
HfO ₂ ^d	$\epsilon^{xx} = \epsilon^{zz}$	5.03	6.58	22.0	12.4	0.124	48.35	0.4835

^aReference [48].^bReference [47].^cDielectric constants and TO mode frequencies from Ref. [13]. Reference [49] has a review of measurements of these TO modes and their damping rates. The damping rates vary between measurements, but all have roughly $\gamma_1/\omega_{\text{TO},1} = \gamma_2/\omega_{\text{TO},2} = 0.01$, which we use.^dDielectric constants and TO mode frequencies from Ref. [13]. Damping rates set to $\gamma_1/\omega_{\text{TO},1} = \gamma_2/\omega_{\text{TO},2} = 0.01$, because we could not find these values extracted previously.

gap between layers that is similar to the layer thickness. All layers are identical, but they are offset to each other, so that a primitive unit cell has to contain atoms from two layers [48]. The individual layers are not completely planar, because the sulfur atoms, which are strongly chemically bonded to each molybdenum atom, are offset in the direction of the c axis [48], Fig. 1(a) of Ref. [3]. The microscopic details of the crystal structure are not necessary for our transport calculations, and, as far as electrostatics are concerned, we treat monolayer MoS₂ as a slab of bulk MoS₂ of width $a = c/2 = 6.145$ Å, Fig. 7. While this is a quite crude description of the atomic structure of MoS₂, it offers the chance to investigate the effects of dynamic screening in these 2D structures.

We treat the electrons in the MoS₂ conduction band minima as truly two-dimensional, that is, we take their wave functions to be delta functions at $z = 0$ in Fig. 5(b), in the middle of the monolayer. Monolayer MoS₂ has two equivalent conduction band minima at the K points (see Fig. 1 of Ref. [29]). Kaasbjerg *et al.* [[29], Fig. 2] fit a parabola to the K -point minimum with good agreement, and comment that the closest conduction band valley lies about 200 meV higher, so that low-field transport is well described by effective mass theory. The effective masses in the longitudinal and transverse directions are almost identical [23,29]. We will use $m^* = 0.35m_e$, which Cheiwchanchamnangij and Lambrecht [23] determined with a self-consistent GW method rather than the value of $m^* = 0.48m_e$, which Kaasbjerg *et al.* [29] obtained with density functional theory and the local density approximation.

B. Results

1. Influence of surrounding dielectrics

We calculate both μ , the dynamically screened interface phonon scattering, and μ_{tot} for MoS₂ surrounded by different dielectrics: a free-standing MoS₂-monolayer, a layer of MoS₂ between layers of hexagonal boron nitride BN, a layer of MoS₂ on SiO₂, and a MoS₂-monolayer between SiO₂ and HfO₂. This is shown in Figs. 8(a) and 8(b).

Hexagonal boron nitride (BN) is mildly anisotropic with $\epsilon'^\infty = 4.5$ and $\epsilon'^0 = 6$, compared to the strongly anisotropic but barely polar MoS₂ with $\epsilon'^\infty = 9.71$ and $\epsilon'^0 = 9.79$. SiO₂ and HfO₂ are isotropic oxides. SiO₂ has $\epsilon^\infty = 2.5$ and $\epsilon^0 =$

3.9, HfO₂, with $\epsilon^\infty = 5.03$ and $\epsilon^0 = 22.0$ is very strongly polar. Details of the dielectric functions are in Table II, and the high-frequency interface dielectric function for each of the four sandwiches has already been plotted in Fig. 6.

The structures SiO₂-MoS₂-vacuum and SiO₂-MoS₂-HfO₂ were investigated experimentally in Ref. [24], the freestanding MoS₂-case is useful as a reference and relevant for studies of the intrinsic, phonon-limited mobility of MoS₂ such as Refs. [26,29]. The BN-MoS₂-BN structure is interesting,

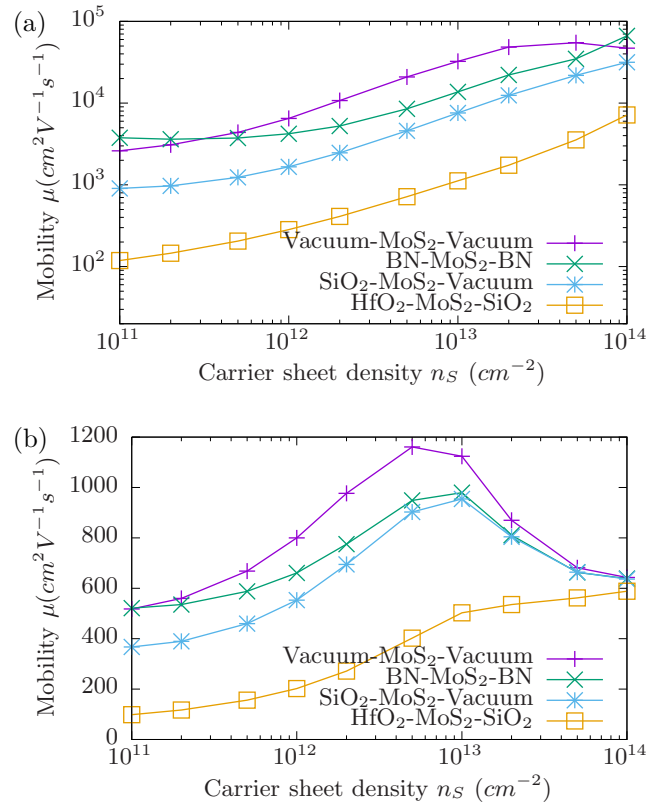


FIG. 8. (a) Mobility limited by dynamically screened interface phonon scattering. (b) Total mobility due to dynamically screened interface phonon scattering, deformation potential and piezoelectric scattering (Appendix E) in different structures, at $T = 300$ K, as a function of carrier sheet density n_s .

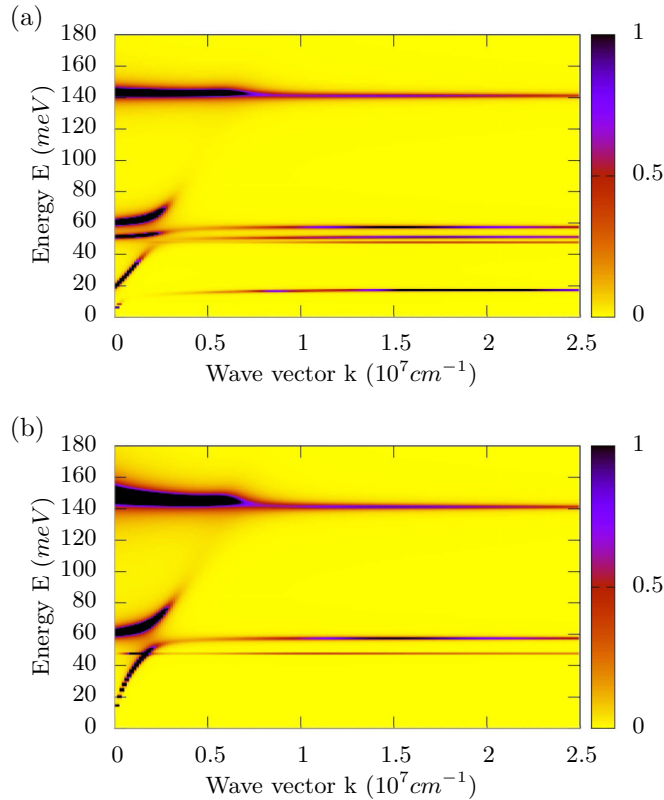


FIG. 9. $\frac{\Im(\epsilon_{\text{interface}})}{|\epsilon_{\text{tot}}|^2} \propto W_{k,\omega}^{0,\text{eff}}/\nu_k$, Eq. (33) as a function of wave vector k and energy $E = \hbar\omega$ for screened interface phonon scattering in the (a) $\text{HfO}_2\text{-MoS}_2\text{-SiO}_2$ structure and (b) $\text{SiO}_2\text{-MoS}_2\text{-vacuum}$ structures at $T = 300$ K and $n = 2 \times 10^{12} \text{ cm}^{-2}$.

because hexagonal BN has a layered structure similar to MoS_2 and its optical phonon frequencies are very high.

Figure 8 shows that the most strongly polar sandwich, $\text{SiO}_2\text{-MoS}_2\text{-HfO}_2$, has the lowest room temperature mobility. HfO_2 also has the lowest TO-phonon energy $\hbar\omega_{\text{TO}} = 12.4$ meV of the considered oxides. The $\text{SiO}_2\text{-MoS}_2\text{-vacuum}$ structure has the next lowest mobility, which is still roughly a factor of 10 larger than that of the $\text{SiO}_2\text{-MoS}_2\text{-HfO}_2$ structure throughout all carrier concentrations. This is because SiO_2 is much less polar than HfO_2 and its lowest TO-phonon energy $\hbar\omega_{\text{TO}} = 55.6$ meV is much higher, even larger than the thermal energy of 25 meV. As the lowest TO-phonon energy in BN is around four times the thermal energy, the mobility of the $\text{BN-MoS}_2\text{-BN}$ structure is higher still, and very similar to mobility of the free-standing MoS_2 .

Figure 9 shows the effect of the different surrounding dielectrics on the effective scattering rate Eq. (33). We can see the hybridized plasmon-phonon modes at long wavelengths, and the flat LO-phonon-like modes at larger wave vectors. The low-energy HfO_2 -like mode and the high-energy SiO_2 -like mode are clearly distinguishable in Fig. 9(a), unlike the remaining modes around 50 meV. We can qualitatively understand that the scattering will decrease if we remove the HfO_2 -type resonances from the effective matrix element in Fig. 9(a), essentially yielding the $\text{SiO}_2\text{-MoS}_2\text{-vacuum}$ $W_{k,\omega}^{0,\text{eff}}$ in Fig. 9(b).

2. Treatment of screening

In this section, we compare carrier mobilities and momentum relaxation times, where the screening of interface polar phonon scattering is treated in different approximations.

(1) The tag “dynamic screening” means fully self-consistent τ_p and $T_{k,\omega}$ from Eq. (D7) and Eq. (D16). The scattering rate in τ_p is calculated from Eq. (57).

(2) The tag “dynamic screening no drag” means fully self-consistent τ_p from Eq. (D7), but the drag term $T_{k,\omega}$ Eq. (D16) is set to zero. The scattering rate in τ_p is calculated from Eq. (57).

(3) The tag “no screening” applies to calculations where the drag term is equally zero (see discussion in Sec. II D 3), but the scattering rate in τ_p is calculated from Eq. (52), i.e., free carriers have no effect on the scattering rate.

(4) The tag “dynamic screening RTA” refers to dynamic screening in the relaxation time approximation. The relaxation time is calculated in a quasielastic approximation according to Eq. (30). The explicit expression is Eq. (D9) in Appendix D. The scattering rate in τ_p is calculated from Eq. (57).

(5) The tag “static screening” also refers to a RTA solution. To obtain the static limit of the relaxation time, we have to replace the scattering rate Eq. (57) with its static limit $W_{k,\omega=0}^0$ and set the phonon dissipation weight factor Eq. (31) to its static limit $C_{k,\omega=0} = 1$ in the momentum relaxation time Eq. (D9) in Appendix D.

In Fig. 10, we calculate the interface phonon scattering limited mobility in the different limits described above, “no screening,” “static screening,” “dynamic screening,” “dynamic screening no drag,” “dynamic screening RTA,” for the layer of MoS_2 on SiO_2 , and the MoS_2 -monolayer between SiO_2 and HfO_2 . Figure 11 shows the relevant scattering rate, Eq. (57), if there is no screening, static, and dynamic screening.

a. Neglecting screening. If one neglects electronic screening altogether, the corresponding interface phonon scattering rate is described by Eq. (52) and looks like Fig. 11(a), where no hybridization effects occur. Qualitatively, and across all systems considered, one can say that for medium and high carrier concentrations, this will overestimate the scattering. We can also see this in plots of the momentum relaxation rate (Fig. 14) or the mobility (Fig. 10).

b. Dynamic screening neglecting phonon drag. Let us illustrate the point we made in Sec. II that not only the change of the scattering rate $W_{k,\omega}^0$ (10) on introduction of free carriers is important, but also the lifetime of the coupled modes the carriers scatter with. Therefore we compare the scattering rate $W_{k,\omega}^0$, Eq. (57), for the $\text{SiO}_2\text{-MoS}_2\text{-vacuum}$ structure [Fig. 11(c)], with the corresponding effective scattering rate $W_{k,\omega}^{0,\text{eff}}$, Eq. (33) [Fig. 9(b)]. The phonon dissipation weight factor Eq. (31), capturing the lifetime of the coupled modes, reduces the striking plasmonlike peaks in Fig. 11(c) to the peaks of Fig. 9(b). Qualitatively speaking, we can infer from a comparison of these plots that a neglect of the phonon dissipation factor would dramatically overestimate the scattering.

On the level of the Boltzmann equation, neglecting the finite lifetime of the coupled modes means neglecting the phonon drag term $G_{k,\omega}$ [Eq. (22), Sec. II]. For a quantitative analysis, we calculate the fully self-consistent, dynamically screened effective momentum relaxation rate neglecting the phonon

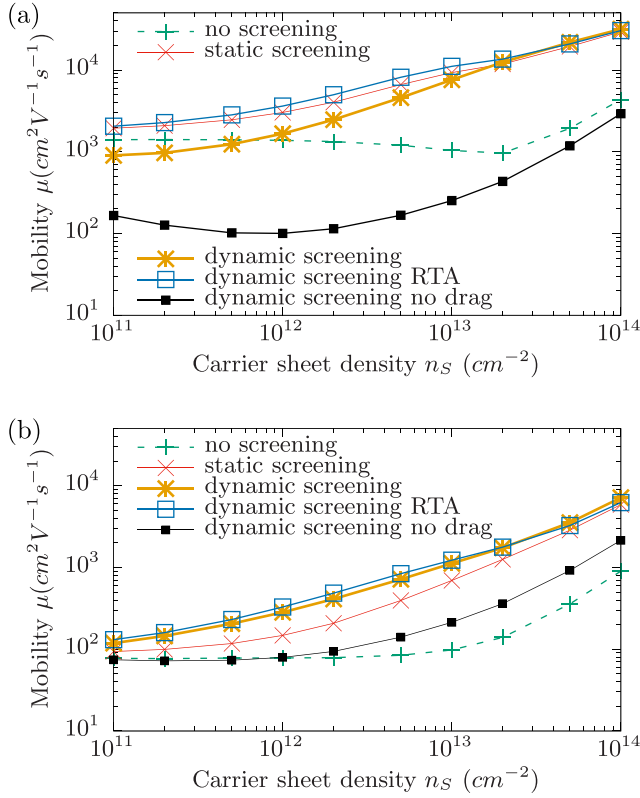


FIG. 10. Room-temperature mobility limited by interface phonon-plasmon scattering in the (a) SiO₂-MoS₂-vacuum and (b) HfO₂-MoS₂-SiO₂ structures as a function of carrier sheet density n_s . Sec. VB 2 explains how the mobilities tagged “no screening,” “static screening,” “dynamic screening,” “dynamic screening RTA,” “dynamic screening no drag,” and “static screening” are calculated.

drag term. Kasiyan and Russu [50] carried out an approximate version of such a calculation. The resulting mobility for the SiO₂-MoS₂-vacuum structure is plotted in Fig. 10(a). As expected, the mobility is much lower than for dynamic screening including phonon drag. Dynamic screening without phonon drag typically [but not always, see HfO₂-MoS₂-SiO₂-sandwich in Fig. 10(b)] yields so-called antiscreening, the effect that scattering is increased, not reduced by the introduction of free carriers.

c. Dynamic screening including phonon drag. Antiscreening in fact exists, but dynamic screening without phonon-drag overestimates it unless the relevant carrier concentrations are close to the intrinsic carrier concentration. For low carrier concentrations, longer-wavelength hybridized modes contribute more to the scattering of carriers. As we can see in Fig. 9, the coupling of the plasmon and phonon modes gives rise to dispersive coupled modes at long wavelengths. The lowest frequencies of these coupled modes have smaller frequencies than the lowest optical modes. If these modes significantly contribute to scattering of carriers, antiscreening can occur. Heuristically speaking, at long wavelengths, the electronic response is slower than the phonon response, so the electrons cannot screen the optical phonon interaction. To the contrary, as these modes have a phonon dissipation factor close to one, they contribute significantly to momentum relaxation.

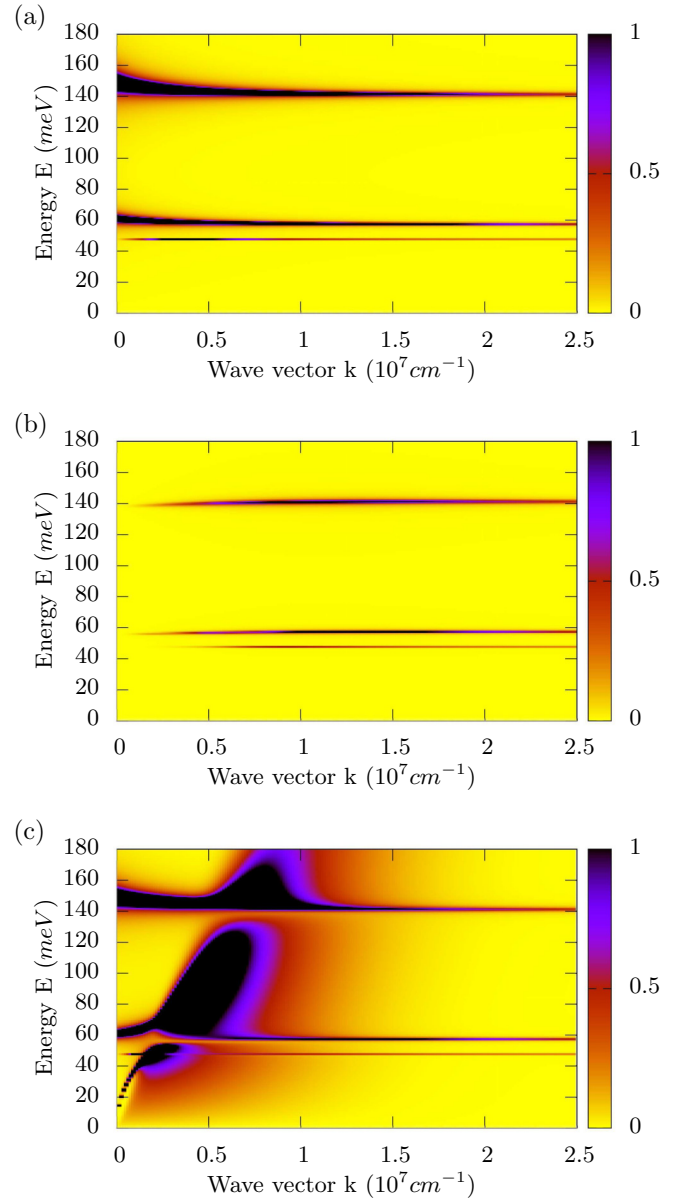


FIG. 11. $\Im m(\frac{-\epsilon^\infty}{\epsilon^c + \epsilon_{\text{interface}} - \epsilon^\infty}) \propto W_{k,\omega}^0 / \nu_k$ Eq. (57) in the SiO₂-MoS₂-vacuum structure at $T = 300$ K and $n = 2 \times 10^{12} \text{ cm}^{-2}$, as a function of wave vector k and energy $E = \hbar\omega$, with different treatments of screening: (a) no screening $\epsilon^c = 0$, (b) static screening $\epsilon^c = \epsilon_{k,\omega=0}^c$ and (c) dynamic screening $\epsilon^c = \epsilon_{k,\omega=0}^{c,\text{RPA}}$.

We can see how antiscreening is captured in the SiO₂-MoS₂-vacuum structure in Fig. 10(a) when we compare the mobility $\mu_{\text{no screening}}$, calculated without screening with the mobility μ_{dynamic} , calculated with dynamic screening. Figure 12(b) shows the ratio $\frac{\mu_{\text{dynamic}}}{\mu_{\text{no screening}}}$ between those mobilities directly. Antiscreening is visible for all the structures except the HfO₂-MoS₂-SiO₂ sandwich, whose lowest TO energy is only roughly half the carrier energy at room temperature. This is because the plasmonlike modes, which are still lower in energy, and which would have to contribute for antiscreening to happen, are low in intensity [see Fig. 9(a)]. See also Fig. 10(b)

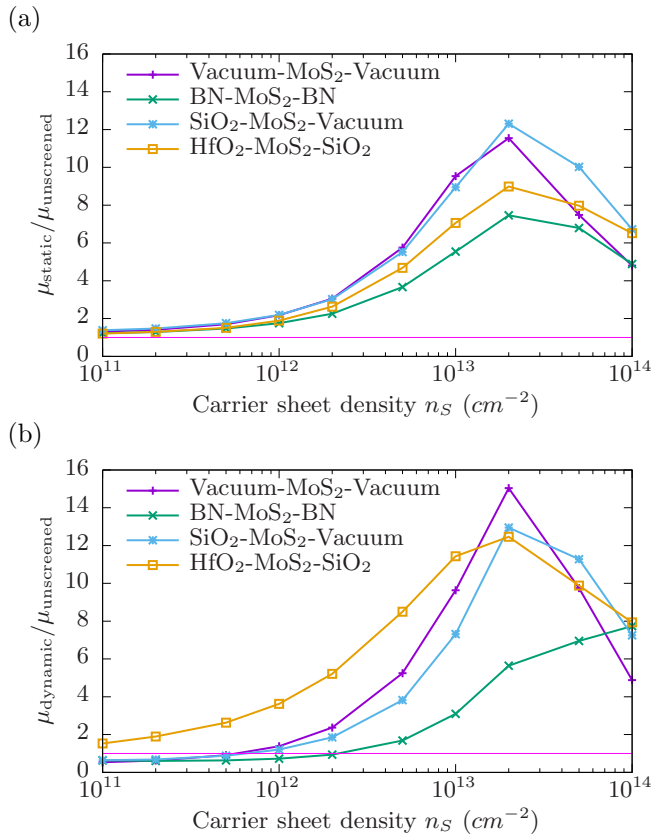


FIG. 12. Ratio between the screened and unscreened interface phonon scattering limited mobilities in different structures at room temperature as a function of carrier sheet density n_S : (a) ratio of the statically screened to the unscreened mobility $\mu_{\text{static}}/\mu_{\text{unscreened}}$ and (b) ratio of the dynamically screened to the unscreened mobility $\mu_{\text{dynamic}}/\mu_{\text{unscreened}}$. Section VB2 explains how the evaluation of the mobilities with “no screening,” “dynamic screening,” and “static screening” differ.

for more detail on the mobility of the $\text{HfO}_2\text{-MoS}_2\text{-SiO}_2$ sandwich.

d. Static screening. By treating screening statically, the hybridization effects for small wave vectors are neglected and the scattering matrix element at the long-wavelength limit is generally decreased. [See the statically screened scattering rate $W_{k,\omega=0}^0$ in Fig. 11(b)]. It is therefore clear that static screening can never describe the antiscreening effect at low carrier concentration. Figure 12(a), showing the ratio $\frac{\mu_{\text{static}}}{\mu_{\text{unscreened}}}$ demonstrates this.

At high carrier concentrations, static screening is often a good approximation, because here, the strongly coupled modes lie at very long wavelengths and hence do not contribute much to momentum relaxation. For intermediate carrier concentrations, the effects on the mobility are generally more subtle.

In Fig. 13(a), we quantify the mistake one would make by treating screening statically by plotting the ratio of the dynamically screened to the statically screened interface phonon scattering mobility for the four different investigated structures. Figure 13(b) does the same, but also takes the other considered contributions to mobility into account

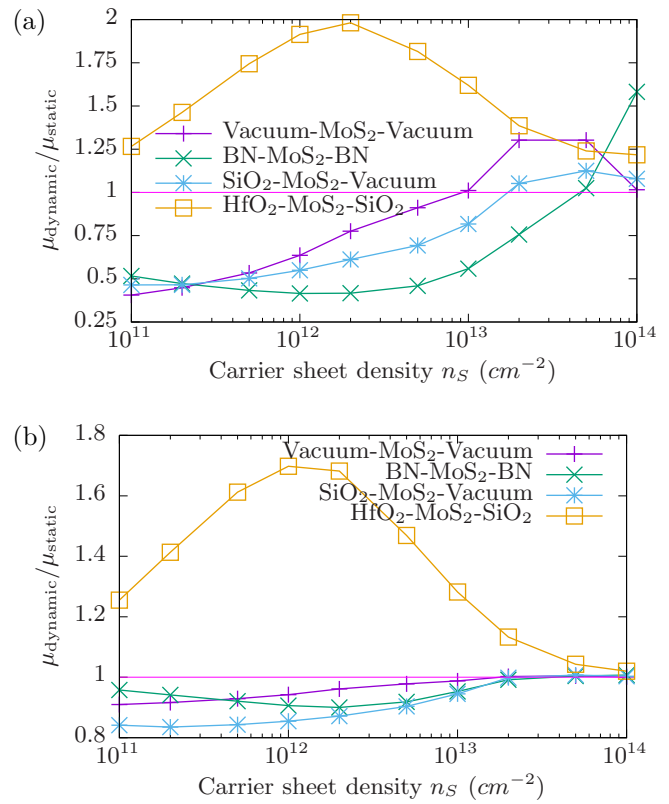


FIG. 13. Ratio of dynamically to statically screened carrier mobility $\mu_{\text{dynamic}}/\mu_{\text{static}}$ in different structures at room temperature as a function of carrier sheet density n_S : (a) interface phonon scattering limited mobility and (b) total mobility (also including deformation potential and piezoelectric scattering, see Appendix E).

(Appendix E). The error is smaller when one takes all other scattering mechanisms (i.e., deformation potential and piezoelectric scattering, see Appendix E) into account, especially for the sandwiches where the interface-phonon-plasmon limited mobility is quite high. [Compare Figs. 13(a) and 13(b).] Even so, statically screening the interface-phonon scattering overestimates the total mobility in the $\text{SiO}_2\text{-MoS}_2\text{-vacuum}$ sandwich by up to 15%, and underestimates the total mobility in the $\text{HfO}_2\text{-MoS}_2\text{-SiO}_2$ sandwich by up to 75%.

e. Effect of screening for different sandwiches. In Fig. 12, we quantify the effect of screening by plotting the ratio of the screened to the unscreened interface phonon scattering mobility for the four different investigated structures. In Sec. III C, we established that the ratio of the screened to the unscreened mobility in the bulk case increased with an increased effective mass of the carriers, and a decrease of the high-frequency dielectric constant. In our X-MoS₂-Y sandwiches, the effective mass is always the same, but their interface dielectric differs. Figure 6 shows the high-frequency limit of the interface dielectric functions of the investigated sandwiches. We see that the rough relation “the higher $\epsilon_{k,\omega \rightarrow \infty}^{\text{interface}}$, the lower $\mu_{\text{screened}}/\mu_{\text{unscreened}}$,” also holds for the height of the peaks in Figs. 12(a) and 12(b). While static screening [Fig. 12(a)] gets the order of the peaks right, it underestimates their magnitude somewhat.

In the bulk case, $\mu_{\text{screened}}/\mu_{\text{unscreened}} < 6$ [Fig. 4(a) in Sec. III C] compared to that for the X-MoS₂-Y sandwiches $\mu_{\text{screened}}/\mu_{\text{unscreened}} < 16$ [Fig. 12(b)], even though the effective masses of ZnS and MoS₂, which have the largest such ratios, are almost identical, and the $\epsilon_{k \approx 1/a, \omega \rightarrow \infty}^{\text{interface}}$ around $ka \approx 1$ and ϵ^∞ are similar. This difference is due to difference of the dielectric response of a three-dimensional compared to a two-dimensional electron gas.

In Sec. III C, Eq. (37), we introduced the critical carrier density n_C where the longitudinal optical phonon frequency and the plasma frequency are equal, and observed that density was roughly where the peak in $\mu_{\text{screened}}/\mu_{\text{unscreened}}$ lay. For the interface phonon case, such a critical carrier density would be more difficult to define, firstly, because there are more optical phonon modes present, and secondly, because the plasma frequency has a linear, not constant, dispersion in the long-wavelength limit. However, we can still see how the peaks in $\mu_{\text{dynamic}}/\mu_{\text{unscreened}}$ in Fig. 12(b) are ordered along the sheet density axes roughly according to the position to their optical phonon frequencies: the HfO₂-MoS₂-SiO₂ sandwich has the lowest TO-phonon frequency and it peaks at the lowest sheet density. The BN-MoS₂-BN sandwich has very high TO-phonon frequencies apart from the TO-frequencies of the weakly polar MoS₂ which all sandwiches share. Note that these shifts are absent in the ratio $\mu_{\text{static}}/\mu_{\text{unscreened}}$ in Fig. 12(a), as static screening is by construction blind to dynamic effects such as the dispersion of the plasma excitations.

3. Relaxation time approximation compared to self-consistent solution of the Boltzmann equation

We observed that for the calculations without screening and with static screening, the relaxation time approximation (RTA) is fairly close to the self-consistent solution for all investigated structures.⁸ This also holds for the calculations with dynamic screening without the phonon drag term.

However, in general, it does not hold for the calculations with dynamic screening including the drag term. The agreement between the RTA and the fully self-consistent solution is good for the mobility calculations in HfO₂-MoS₂-SiO₂ [Fig. 10(b)], but not for the other investigated structures.

In particular, the RTA does not capture antiscreening, as can be seen in Fig. 10(a). Explicitly this means, the hybridized modes in $W_{k,\omega}^{0,\text{eff}}$, Eq. (33), in Fig. 9 do not contribute significantly to scattering in the RTA. However, they do contribute critically in the fully self-consistent solution. One can see that in Fig. 14, which illustrates the difference between the effective momentum relaxation rate, calculated with “no screening,” “static screening,” “dynamic screening,” “dynamic screening no drag,” “dynamic screening RTA,” for the SiO₂-MoS₂-vacuum structure: the fully self-consistent effective momentum relaxation rate (marked “dynamic screening”) is larger than its RTA correspondent (marked “dynamic screening RTA”) for energies smaller than 60 meV, where hybridization occurs, and smaller for energies over 60 meV,

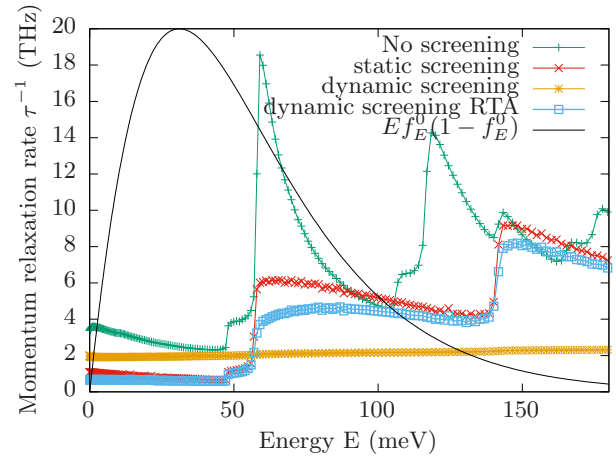


FIG. 14. Momentum relaxation rate calculated with different treatments of screening, as a function of electron energy E , for a SiO₂-MoS₂-vacuum structure at $T = 300$ K and $n = 2 \times 10^{12}$ cm⁻². Section V B 2 explains how the momentum relaxation rates $\frac{1}{\tau}$ tagged “no screening,” “dynamic screening,” “dynamic screening RTA,” “dynamic screening no drag,” and “static screening” are calculated.

where hybridization is less important. The fully self-consistent effective momentum relaxation rate shows none of the steps associated with a certain onset of the emission of optical phonons, seen very strongly in the unscreened curve, and to a lesser extend in the static screening and dynamic screening in RTA curve. This flatness is another indication that the coupling to plasmons, which are dispersive and hence produce less featured momentum relaxation rates, are more important in the fully self-consistent effective momentum relaxation time than in the RTA.

The iteration to self-consistency is a process to find the right balance between the case where all the coupled modes relax momentum (no drag term), and the case where the carriers do not contribute to momentum relaxation at all (no screening case). The RTA is a somewhat reasonable approximation but fails to address finer details of the full solution.

Keeping in mind that $W_{k,\omega}^{0,\text{eff}}$, Eq. (33), only strictly has meaning within the RTA, it still conveys some intuition for the qualitative effects of dynamic screening. However, our calculations show that, in general, the RTA is no viable shortcut, and it is necessary to find the fully self-consistent effective momentum relaxation time to capture dynamically screened interface-phonon scattering correctly.

4. Present work compared to previous studies

Simulations of the carrier mobility in MoS₂ have mainly been of one of the following two types: the first kind treat freestanding single layers of MoS₂ from first principles, e.g., Refs. [26,29,51]. Such calculations aim to predict the “intrinsic” carrier mobility, due to scattering with the monolayer MoS₂ phonons. The second kind focusses on other scattering mechanisms, which limit the mobility in realistic devices, taking into account impurities, and the type and dimensions of the surrounding dielectrics [25,27,28]. The methodology there tends to rely on effective mass theory and macroscopic electrostatics, though the parameters might

⁸In all plots, we show the no screening case in the self-consistent solution, but the static screening case in the RTA, because the previous study by Ma and Jena [25] used static screening and the RTA.

be obtained from electron [23,29] and phonon [52,53] band-structure calculations. Free carrier screening, present due to the impurity doping of nonideal samples of MoS₂ or due to gating in FETs, falls into the second type of treatment.

Kaasbjerg *et al.* [26,29] calculated the intrinsic mobility in a free-standing layer of MoS₂. They performed first-principles electronic structure calculations to obtain the relevant scattering matrix elements in the low carrier concentration limit. However, rather than accounting for the free-carriers effects explicitly in another *ab initio* calculation, they take screening into account *ad hoc* by dividing their $n \rightarrow 0$ matrix elements by appropriate model dielectric functions [26].

Ma and Jena [25] published a study of the mobility of different structures consisting of MoS₂ surrounded by different dielectrics, using model dielectric functions to statically screen the matrix elements calculated by Kaasbjerg *et al.* [26]. While lacking the detail of a microscopic dielectric function, these numerically cheap model dielectric functions can capture the electrostatic effects of placing a monolayer of MoS₂ between a large number of permutations of different dielectrics.

This work uses Kaasbjerg *et al.*'s "screening by hand" approach for composite structures, as Ma and Jena [25] have. In methodology, it is very similar to Ma and Jena's, in that it also applies single particle transport and macroscopic electrostatics to MoS₂-heterostructures. However, it uses the formalism established in Secs. II and IV to focus particularly on the screening of the interface phonon scattering effect, which is important in polar MoS₂ heterostructures.

a. Comparison of present work with calculations from Ma and Jena [25]. In this section, we compare some of our results with some results from the literature. Out of the studies discussed above, Refs. [26,29,51] give calculation of the carrier mobility as a function of the sheet carrier density, but only for MoS₂ suspended in a vacuum, and neglecting screening. We therefore compare our results with some presented by Ma and Jena [25]. In their Fig. 7(b), they present calculations of a mobility due to statically screened interface phonon scattering, charged impurity scattering, acoustic and optical deformation potential scattering, and LO-phonon scattering, as a function of carrier sheet density at room temperature. The impurity concentration is fixed at $N_I = 10^{11} \text{ cm}^{-2}$. This mobility is plotted against some of our own calculations for a HfO₂-MoS₂-SiO₂ structure in Fig. 15. We choose the HfO₂-MoS₂-SiO₂ structure, because its mobility is dominated by screened polar interface phonon scattering, the scattering mechanism we are particularly interested in in this paper. We include other scattering mechanisms (acoustic and optical deformation potential scattering and piezoelectric scattering, as discussed in Appendix E), but they have barely any influence on the total mobility. The effect of neglecting charged impurity scattering, which we have not included, should also be negligible for $N_I = 10^{11} \text{ cm}^{-2}$. We can see this from Ma and Jena's, [25] [Fig. 7(a)] calculations for $n_S = 10^{13} \text{ cm}^{-2}$ and $N_I = 10^9 \text{ cm}^{-2}$, which we included in Fig. 15 as a diamond. It lies on the line for the mobilities with a $N_I = 10^{13} \text{ cm}^{-2}$ impurity concentrations for the HfO₂-MoS₂-SiO₂ structure.

Figure 15 compares calculations of the total room temperature mobility in a HfO₂-MoS₂-SiO₂ structure as a function

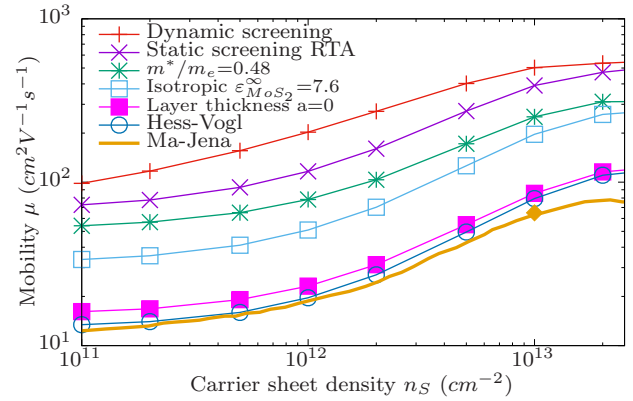


FIG. 15. Room-temperature mobility in a HfO₂-MoS₂-SiO₂ structure as a function of carrier sheet density. The thick orange solid line is from a calculation by Ma and Jena [25]. All other curves are from our calculations. The top red line with the crosses marked "dynamic screening" is our best description of the mobility in the HfO₂-MoS₂-SiO₂ structure, and was first presented in Fig. 8(b). Each successive curve is marked with the additional assumption that has been made to calculate it, as explained in Sec. VB 4.

of carrier sheet density by Ma and Jena [25] to ours. Ma and Jena's treatment of screened interface polar phonon scattering differ from ours in several important points. In order to disentangle the effects of these differences on the mobility from each other, we go step by step: We start with the calculation which we believe to best describe screened polar interface phonon scattering in the HfO₂-MoS₂-SiO₂ structure. We then change our treatment to agree with that by Ma and Jena [25], eliminating one difference at a time. Each change will be discussed first, and then retained for all subsequent calculations. Incidentally, each of these changes reduces the mobility by a certain amount, until we finally reproduce Ma and Jena's mobilities, which are around an order of magnitude lower than our "dynamic screening" results from Fig. 15, quite accurately.

(1) Dynamic screening. Our best description of interface polar phonon scattering involves dynamic screening as discussed in Sec. VB 2. This curve was first presented in Fig. 8(b), and is marked "dynamic screening" in Fig. 15.

(2) Static screening and the RTA. Ma and Jena [25] employ static screening and the relaxation time approximation. We include our calculation with static screening and the RTA in Fig. 15 marked "static screening RTA." As shown in Fig. 13(b), using static rather than dynamic screening decreases the mobility by up to 43%. All calculations described below also employ static screening and the RTA.

(3) MoS₂ effective mass. Ma and Jena use the LDA effective mass of $m^* = 0.48m_e$ [29]. We used a *GW* effective mass of $m^* = 0.35m_e$ [23], because *GW* band structures compare more favorably with experiment than those calculated in the LDA (cf. Ref. [54] and references therein). From here on, we will use the LDA value of $m^* = 0.48m_e$, like Ma and Jena. This causes the mobility to decrease by about 25% to 35% throughout all carrier densities.

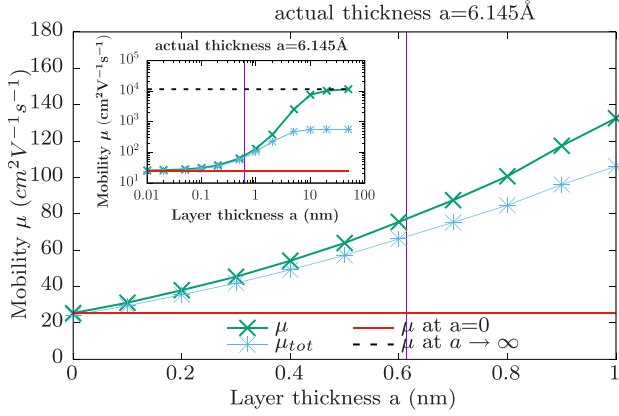


FIG. 16. Dependence of the mobility μ due to unscreened polar interface phonon scattering and the total mobility μ_{tot} on the thickness a of the interface layer in structures of the type described in Fig. 5(b). This plot is for a HfO_2 - MoS_2 - SiO_2 structure at room temperature and a carrier sheet density $n_s = 10^{11} \text{ cm}^{-2}$. The main plot shows layer thicknesses around the actual thickness of MoS_2 of $a = 6.145 \text{ \AA}$, while the inset shows how the mobilities when a is varied over several orders of magnitude.

(4) Isotropic dielectric constant of MoS_2 . Ma and Jena use an isotropic dielectric constant of MoS_2 of 7.6.⁹ We use a formalism (Sec. IV B) which accounts for the anisotropic dielectric functions of MoS_2 . Our effective scalar high-frequency constant for MoS_2 $\epsilon'_{\text{MoS}_2} = 9.7$, see Table II and Eq. (45). Taking Ma and Jena's isotropic dielectric constant decreases the mobility by between 38% at low carrier sheet density and 20% at high carrier concentration.

(5) Interface layer thickness. Ma and Jena use an expression for the polar interface phonon scattering limited mobility which only holds if the MoS_2 -interface layer is infinitely thin, $a = 0$. We account for a finite layer thickness $a = 6.145 \text{ \AA}$, see Sec. IV B. Figure 16 shows how, according to our continuum model, the unscreened polar interface scattering limited mobility would vary if it was possible to change the thickness of a monolayer of MoS_2 at will. The inset demonstrates that the mobility would change drastically if one were able to vary the layer thickness by several orders of magnitude. The main figure shows that changes of the layer thickness by a fraction of an \AA around our value of $a = 6.145 \text{ \AA}$, a realistic guess for the uncertainty of a , has much smaller effects on the mobility. Still, setting $a = 0$, as Ma and Jena do, reduces the mobility by a more than a factor of two for all the considered n_s .

(6) Hess and Vogl treatment. Ma and Jena treat the HfO_2 - MoS_2 - SiO_2 structure with Hess and Vogl's expression for interface polar phonon scattering (discussed in Sec. IV B). Here, this means “switching off” the polar phonons in SiO_2 by fixing the silica dielectric function at its high-frequency limit, ignoring the electrostatics of the MoS_2 layer, and only considering the lowest frequency polar phonon in HfO_2 . This

reduces the mobility further to give very good agreement with Ma and Jena's calculation.

Implementing all these changes gives excellent agreement between our mobility calculations and those by Ma and Jena [25] at low carrier sheet densities. Ma and Jena's slightly lower mobilities at high carrier sheet densities could be due to an inconsistency of their treatment of electrostatics in screening. While they neglect the MoS_2 thickness in their treatment of unscreened interface polar phonon scattering, they take it into account in their generic treatment of screening of all scattering processes. Another possible cause for the slight discrepancy are differences in the treatment of other scattering mechanisms (Appendix E). We checked that our different treatment of the electronic wave functions in the transverse directions (Ma and Jena have particle in a box wave functions, and we delta functions) amounts to less than a 3% difference in the mobility at any n_s .

VI. CONCLUSIONS

One aim of this paper was to develop a formalism which describes momentum relaxation due to carriers scattered by longitudinal plasma excitations and by longitudinal optical phonons on an equal footing, because these two excitations are in general coupled. The other aim was to investigate this in two-dimensional structures involving MoS_2 sandwiched between different dielectrics.

We achieved this by putting particular focus on the effect of the nonequilibrium collective excitations in the coupled Boltzmann equations for collective longitudinal excitations and carriers. This term is known as the “phonon drag” term in the context of thermal conductivity [8]. We improved on previous models [7,13,17,50] by including the anharmonic lifetime of the coupled collective excitations. If carriers transfer momentum into a collective mode with an anharmonic lifetime which is much longer than the carrier-collective mode relaxation time, the collective mode will likely not decay before it can transfer the momentum back to the carriers. Conversely, if carriers transfer momentum into a collective mode with an anharmonic lifetime, which is much shorter than the carrier-collective mode relaxation time, it will likely decay almost immediately, and the carrier momentum will be lost. Conventionally, carrier-plasmon scattering has been treated in the infinite lifetime limit, and carrier-LO-phonon scattering in the zero lifetime limit. Previous authors have struggled with treating carrier scattering with coupled plasmon-LO-phonon modes in terms of those limits [11,13]. Our approach naturally overcomes these struggles by assigning a finite lifetime to each of the coupled collective modes.

Moreover, we propose a new way of identifying the nature of the coupled modes. Varga's phonon content [10] only determines how phononlike or plasmonlike a coupled mode is in the long-wavelength limit. Our solution naturally introduced the phonon dissipation weight factor, the ratio between the imaginary part of the lattice dielectric function and the imaginary part of the total dielectric function. This quantity lets us assess how phononlike or plasmonlike the coupled excitations behave at a certain frequency and at any wave vector when it comes to degradation of an electric current.

⁹They do not specify if this is supposed to be ϵ^∞ or ϵ^0 , but as the LO-TO splitting in MoS_2 is very small [52,53], this does not matter much.

While our fully self-consistent solutions to the Boltzmann equation require some numerical effort, our method also yields formulas for the effective momentum relaxation time which are as simple to use as those by Kim *et al.* [11]. The calculations in the present work were carried out assuming a perfectly parabolic, spherical conduction band. An extension of our approach to materials with nonparabolic and elliptical bands would be conceptionally straightforward, if computationally cumbersome.

When we applied our approach to dynamically screened electron-LO-phonon scattering in bulk polar semiconductors, we observed that the mobility limited by coupled collective mode scattering is most increased compared to mobility limited by pure LO-phonon scattering at a density where the plasma frequency is similar to the optical phonon frequencies. Calculations for a variety of direct gap polar semiconductors assuming a single, spherical conduction band indicate that this increase is strongest for materials with large effective mass and small high-frequency dielectric constant.

Finally, we applied our approach to screened remote phonon scattering in structures where a monolayer of molybdenite lies between different polar oxides. We found that the difference between screened remote phonon scattering (i.e., coupled collective mode scattering) and unscreened remote phonon scattering is strongest for heterostructures with a small high-frequency interface dielectric function, which is an insight that carries over from the bulk case. Our fully self-consistent dynamically screened remote phonon scattering calculation can capture antiscreening at low carrier concentration, unlike previous calculations of remote phonon scattering, which used static screening and the RTA [25]. Using static screening leads to an overestimation of the total mobility by up to 15% at low electron concentrations around $n_S = 10^{11} \text{ cm}^{-2}$ in devices with a molybdenite monolayer on silica, due to the neglect of antiscreening. In devices with a monolayer of molybdenite between hafnia and silica, static screening can underestimate the mobility by up to 75% at intermediate carrier concentrations around $n_S = 10^{12} \text{ cm}^{-2}$. At high carrier concentrations, the agreement between static and dynamic screening is good. Given these findings, we recommend carrying out a fully self-consistent dynamically screened LO-phonon or remote phonon scattering calculation including phonon drag if the LO-phonon or remote phonon scattering contributes significantly to the total mobilities, and the relevant carrier concentrations are in an intermediate regime.

We also demonstrated that taking the thickness of the MoS_2 layer into account as far as electrostatics are concerned is important for the mobility. It changes the mobility of a structure with a monolayer of MoS_2 between hafnia and silica by more than a factor of two for all considered carrier sheet densities. Whether our continuum model gives an accurate description of the electrostatics of such a small-scale structure is another question. It would be interesting to see dielectric functions for the composite structures discussed here calculated from first principles, taking into account the detailed atomistic structure of the heterostructure.

ACKNOWLEDGMENT

This work was supported by Science Foundation Ireland through Grant 12/IA/1601.

APPENDIX A: TREATMENT OF CARRIER-COUPLED MODE SCATTERING IN LIMITING CASES

In this section, we show that the method presented in Sec. II contains previous descriptions of the long-wavelength-limit [10–12] as its long-wavelength limit. We also demonstrate how Fischetti *et al.*'s approximate treatment of Landau damping [13] compares to our approach, which has Landau damping built in.

We discuss these limits in the three-dimensional case of bulk polar semiconductors, rather than the 2D case (interface or remote phonon scattering) because its comparative simplicity gives a clearer view of the basic physics involved. As our approach contains all the relevant information about the system in the dielectric function, this means making approximations to the dielectric function. These approximations often are that the imaginary part of the dielectric function vanishes in a certain region. As the scattering rate $W_{k,\omega}^0$ from Eq. (10) has the form of the Poisson representation of the delta function for small $\Im\{\varepsilon^{\text{tot}}\}$, we see that when the imaginary part of the dielectric function vanishes, $W_{k,\omega}^0$ becomes a delta function at the zeros of the real part of the dielectric function,

$$\begin{aligned} \frac{1}{\pi} \Im\left(\frac{-1}{\varepsilon_{k,\omega}^{\text{tot}}}\right) &\longrightarrow \delta(|\Re(\varepsilon_{k,\omega}^{\text{tot}})|) \\ &= \sum_i \frac{\delta(\omega - \omega_k^i)}{|\frac{\partial}{\partial \omega} \Re(\varepsilon_{k,\omega}^{\text{tot}})|} \text{ for } \Im(\varepsilon^{\text{tot}}) \rightarrow 0, \end{aligned} \quad (\text{A1})$$

where ω_k^i are the zeros of the total dielectric function. Consequently, the treatment of the problem is now in terms of discrete modes rather than a continuous spectrum, and it will be convenient to describe the scattering in terms of the scattering strength F^i of each mode i than in terms of the continuous scattering rate $W_{k,\omega}^0$:

$$W_{k,\omega}^0 = \sum_i \frac{2\pi}{\hbar} F_k^i \delta(\omega - \omega_k^i). \quad (\text{A2})$$

1. Long-wavelength limit

As mentioned in Sec. III B 1, the phonon dissipation weight factor goes to 1 in the long-wavelength limit, so that the scattering rate and the effective scattering rate show the same long-wavelength behavior. Consequently, we only have the behavior of the scattering rate as $k \rightarrow 0$ left to consider, where

$$\varepsilon_\omega^c = \varepsilon^\infty - \frac{\omega_P^2}{\omega^2} \quad (\text{A3})$$

with the plasma frequency $\omega_P = \sqrt{\frac{4\pi e^2 n}{\varepsilon_\infty m^*}}$ in a semiconductor with effective mass m^* , the elementary charge e , high-frequency dielectric function ε^∞ , and carrier concentration n [12,38]. As discussed in Sec. III A 2, the phonon dielectric function Eq. (1) is already in the long-wavelength limit. If we also set the damping rate γ to zero, $\Im(\varepsilon^{\text{tot}}) \rightarrow 0$, and the scattering rate becomes infinitely sharply peaked at $\Re(\varepsilon_{\omega_\pm}^{\text{tot}}) = 0$ and we can obtain the coupled mode frequencies

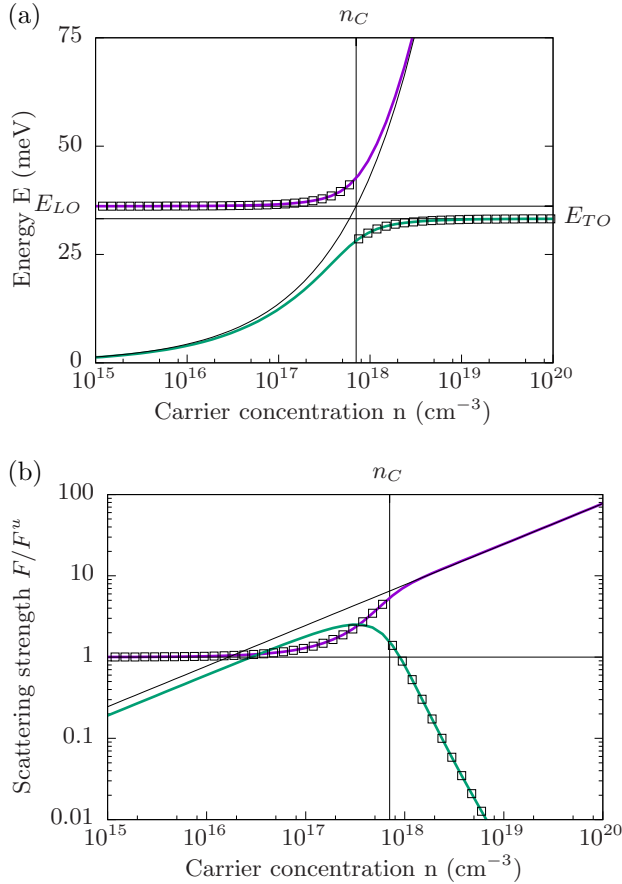


FIG. 17. (a) Coupled mode frequencies in n -type GaAs in the long-wavelength limit (thick lines), as a function of carrier concentration. Additional grid lines mark the LO- and TO-phonon energy. The thin line indicates the plasma dispersion. (b) Carrier scattering strength of the coupled modes Eq. (A5) (thick lines), the plasma mode Eq. (A7) (thin), as a function of carrier concentration, all divided by the LO-phonon scattering strength. Both plots have a grid line marking the critical density n_C , where $\omega_p = \omega_{LO}$. The more phononlike of the two coupled modes is marked with open squares.

ω_{\pm} from a biquadratic equation [10]

$$\omega_{\pm}^2 = \frac{1}{2}(\omega_{LO}^2 + \omega_p^2) \pm \frac{1}{2}\sqrt{(\omega_{LO}^2 + \omega_p^2)^2 - 4\omega_p^2\omega_{TO}^2}. \quad (A4)$$

These coupled mode frequencies are shown in Fig. 17(a) for a range of carrier concentrations in n -GaAs. The scattering strength for each coupled mode is the screened Fröhlich scattering strength

$$F^{\pm} = v_k \frac{\pi \omega_{\pm}}{2\epsilon_{\infty}} \frac{\omega_{\pm}^2 - \omega_{TO}^2}{\omega_{\pm}^2 - \omega_{\mp}^2} \quad (A5)$$

introduced by Kim *et al.* [11]. The last fraction in Eq. (A5) is always positive. Equivalent expressions for the long-wavelength scattering strength Eq. (A5) have been derived by Ridley [12] and Fischetti *et al.* [13].

The long-wavelength limit for coupled modes-scattering includes LO-phonon-scattering as the $\omega_p \ll \omega_{LO}$ limit, and the corresponding unscreened Fröhlich scattering

strength is [11]

$$F^u = v_k \frac{\pi \omega_{LO}}{2} \left(\frac{1}{\epsilon_{\infty}} - \frac{1}{\epsilon_0} \right). \quad (A6)$$

For comparison with carrier-plasmon scattering, we introduce the plasmon scattering strength

$$F^p = v_k \frac{\pi \omega_p}{2\epsilon_{\infty}}. \quad (A7)$$

We show these different scattering strengths for a range of carrier concentrations in n -type GaAs in Fig. 17(b).

2. Strong electronic screening limit

In cases where $\omega_p \gg \omega_{LO}$, the carrier dielectric function is often approximated by the Thomas-Fermi limit:

$$\epsilon_k^c = \epsilon^{\infty} \left(1 + \frac{k_{TF}^2}{k^2} \right), \quad (A8)$$

where $k_{TF} = \sqrt{\frac{4}{\pi k_F a_0^*}} k_F$ is the Thomas-Fermi wave vector, e.g., Ref. [55]. Assuming that $\gamma = 0$, this yields a delta-peak scattering rate at the frequency

$$\omega_k^{TF} = \sqrt{\frac{\omega_{TO}^2 + \frac{k^2}{k_{TF}^2} \omega_{LO}^2}{1 + \frac{k^2}{k_{TF}^2}}} \quad (A9)$$

with the scattering strength

$$F_k^{TF} = v_k \frac{\pi}{2\epsilon_{\infty} \omega_k^{TF}} \frac{[(\omega_k^{TF})^2 - \omega_{TO}^2]^2}{\omega_{LO}^2 - \omega_{TO}^2}. \quad (A10)$$

In this approximation, the frequency of the single relevant mode goes from ω_{TO} at $k = 0$ to ω_{LO} at $k \rightarrow \infty$, while the scattering strength goes from zero to the LO-phonon value Eq. (A6), see Figs. 2(c) and 18.

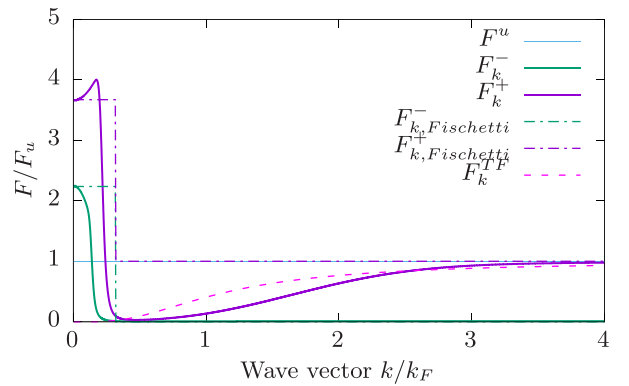


FIG. 18. Comparison of discretized scattering strengths Eq. (A13) to the scattering strengths from Sec. A3 for $n = 5 \times 10^{17} \text{ cm}^{-3}$ at room temperature, depending on the wave vector scaled by the Fermi wave vector, k/k_F . All scattering strengths are plotted as multiples of the carrier-LO-phonon scattering strength F^u .

3. Approximation of Fischetti *et al.*

The long-wavelength approximation discussed above gives simple convenient expressions, but it neglects the dispersion and the damping of the modes. The latter issue is addressed by Fischetti *et al.* [13]. Their approximation was developed for two-dimensional structures, but it can be applied to three-dimensional cases. They approximately treat the plasma modes as damped out entirely as soon as they enter the single pair excitation regime in the degenerate limit (see footnote 1, p. 2).

In the present case, Fischetti *et al.* [13]’s method only uses the coupled modes for wave vectors shorter than the wave vector where the plasmonlike mode enters the single pair excitation regime (see Appendix A 5). The plasmonlike mode with frequency ω_c is defined by

$$\omega_c = \begin{cases} \omega_+ & S_+ \leq S_- \\ \omega_- & S_- < S_+ \end{cases}. \quad (\text{A11})$$

To determine which of the two modes ω_{\pm} is more plasmonlike or phononlike, Fischetti *et al.* use Varga’s “phonon content” [10,11] S_{\pm} , which is discussed in Appendix A 5. In the case of only two coupled modes in the 3D case, the plasmonlike mode is the lower mode if $n < n_c$ and the upper mode if $n > n_c$ (see Fig. 17). This makes the wave vector where ω_c enters the single pair excitation region: $k_c = k_F(\sqrt{\frac{\hbar\omega_c}{E_F} + 1} - 1)$.

For $k > k_c$, only the LO-phonon mode is considered. This means that the plasmonlike mode disappears when it reaches the single pair excitation regime. The frequency of the phononlike mode jumps from ω_{\pm} to ω_{LO} at $k = k_c$ (Fig. 3). The scattering strengths for the Fischetti approximation $F_{k,\omega}^{\pm}$ consequently jump from the long-wavelength expression Eq. (A5) to the Fröhlich expression Eq. (A6) at $k = k_c$:

$$F_{k,\text{Fischetti}}^{\pm} = \begin{cases} F^{\pm} & k \leq k_c, \\ F^u & k > k_c \text{ and } \omega_{\pm} \neq \omega_c, \\ 0 & \text{else.} \end{cases} \quad (\text{A12})$$

In Fig. 3, we plot the coupled modes in this approximation for GaAs with an electron density of $n = 5 \times 10^{17} \text{ cm}^{-3}$, together with the phonon dissipation factor at zero temperature, $C_{k,\omega}^{T=0}$. $C_{k,\omega} = 1$ on the long-wavelength side of the single-pair excitation limit, indicating that there, the carrier-coupled mode scattering is fully dissipative, just as for electron-phonon scattering. Fischetti’s approximation incorporates this, only the cutoff for the single-pair excitation regime is chosen somewhat more simply. Hence it is the only approximation discussed which reflects the importance of the lifetime of the coupled modes for the scattering rate, although indirectly. Fischetti’s approximation, however, does not capture the situation inside the single pair excitation region accurately. We will discuss this in more detail in the following section.

4. Discretization of continuous effective scattering rate

In order to compare the limiting cases from Secs. A 1, A 2, and A 3, with the relaxation time approximation to the full solution from Sec. II D 2 on the level of the scattering strengths,

we define the discretized effective scattering strength

$$F_k^{\pm} = \frac{\hbar}{2\pi} \int_{\omega_k^{\pm} - \Delta\omega}^{\omega_k^{\pm} + \Delta\omega} d\omega W_{k,\omega}^{0,\text{eff}} \quad (\text{A13})$$

with $W_{k,\omega}^{0,\text{eff}}$ from Eq. (33). The exact width $\Delta\omega$ of the integration interval is not crucially important, as the effective scattering rate has two well-defined peaks—see Fig. 2(c)—but it must be large enough to capture each peak. Figure 18 shows the discretized scattering strengths calculated in this manner. Also shown are F^u Eq. (A6), F_k^{TF} Eq. (A10), and $F_{k,\text{Fischetti}}^{\pm}$ Eq. (A12).

$F_{\text{Fischetti}}^+$ is equal to F^u throughout the single pair excitation regime, while F_k^+ is very small at the low k side of the single pair excitation region and only grows towards F^u as it leaves the single pair excitation region again. The Thomas-Fermi scattering strength F_k^{TF} , however, shows good qualitative agreement with the F^{\pm} . An approximation similar to Fischetti *et al.* [13], but with the scattering strength inside the single pair excitation region described by F_k^{TF} rather than F^u would improve the qualitative behavior while retaining much of the simplicity of the approximation.

5. Approximate treatment of carrier-coupled mode scattering in the long-wavelength limit

a. Phonon content of the coupled modes. A concept called “phonon content” is often invoked to describe the character of the coupled modes. It was first introduced by Varga [10]. We will use the phrase as in Kim *et al.* [11], and also use their notation, which is simpler than the equivalent expression used by Ridley [12]. The phonon content is the fraction of kinetic energy of the coupled modes that falls to the share of the lattice. It can be expressed as

$$S_{\pm} = \frac{\omega_{\pm}^2 - \omega_P^2}{\omega_{\pm}^2 - \omega_{\pm}^2}, \quad (\text{A14})$$

while the Varga phonon content is $S_{\pm}^V = \frac{\omega_{LO}}{\omega_{\pm}} S_{\pm}$. Varga [10] also remarked that the phonon content of both modes sums up to one. Therefore we now call $1 - S_{\pm}$ the plasmon content of the mode. This allows us to say that a mode is, say 60% phononlike and 40% plasmonlike, as the upper mode in GaAs for $n = 5 \times 10^{17} \text{ cm}^{-3}$. The phonon content of the coupled modes in GaAs is shown in Fig. 17(a) for different carrier densities. We note that the concept of phonon content is limited to well-defined modes.

b. Single pair excitation region. This is the region in a wave-vector-energy plane where energy and quasimomentum conservation allow the plasma excitation to decay into an electron-hole pair. Note that in the present context, these are quasielectrons and holes in the degenerate carrier gas, which is used as a model for the conduction/valence band of an n type/ p type). The phrase is used to distinguish from a regime, in which multiple pairs can be excited, e.g., Ref. [31]. When expressed in terms of Fermi energy and wave vector, the long-wavelength boundary of the single pair excitation regime is at $\frac{E}{E_F} = \frac{k}{k_F}(\frac{k}{k_F} + 2)$, and the short-wavelength boundary is at $\frac{E}{E_F} = \frac{k}{k_F}(\frac{k}{k_F} - 2)$. These boundaries are marked in Figs. 1–3.

APPENDIX B: ITERATION PROCEDURE

It is evident that Eq. (27) cannot be solved analytically for τ_p , because it involves both τ_p and integrals over τ at different wave vectors. We will therefore find a solution iteratively: we multiply Eq. (27) by τ_p and write the resulting equation as

$$1 = \tau_p R_p^1 - R_p^2\{\tau\} + R_p^3\{\tau\}, \quad (\text{B1})$$

where R_p^1 , $R_p^2\{\tau\}$, and $R_p^3\{\tau\}$ are the first, second, and third terms in Eq. (27) multiplied by τ_p . The curly braces indicate that $R_p^2\{\tau\}$ and $R_p^3\{\tau\}$ are functionals of τ_p . We choose

$$\tau_p^{n+1} = \frac{1}{R_p^1} (1 + R_p^2\{\tau^n\} - R_p^3\{\tau^n\}) \quad (\text{B2})$$

as an iteration procedure. If $\tau_p^n \rightarrow \tau_p$, it will fulfill Eq. (23). Other iteration procedures are conceivable, and should yield the same solutions, but the present one has proved very numerically stable even for undamped iteration.

APPENDIX C: EFFECTIVE MOMENTUM RELAXATION TIME FOR MATERIALS WITH SPHERICAL PARABOLIC BANDS: 3D

The linearized collisional integral has been evaluated explicitly by Sanborn [17] for pure carrier-carrier scattering and in bulk semiconductors with spherical parabolic bands. Apart from the scattering rates, our expression is entirely equivalent to hers. However, we give the expression in terms of transferred energy and wave vector, while she uses bipolar coordinates [56].

We start by making the approximation of spherical parabolic bands, $E_p = E_p = \frac{\hbar^2 p^2}{2m^*}$, from which follows $\mathbf{v}_p = \frac{\hbar}{m^*} \mathbf{p}$ for the group velocity, and $\tau_p = \tau_p$. We scale all wave vectors with the Fermi wave vector $k_F = \sqrt[3]{3\pi^2 n}$ and all energies with the Fermi energy $E_F = \frac{\hbar^2 k_F^2}{2m^*}$ to obtain dimensionless wave vectors and energies. Explicitly, this gives $\Omega = \frac{\hbar\omega}{E_F}$, $K = \frac{k}{k_F}$, $P = \frac{p}{k_F}$, and $Q = \frac{q}{k_F}$. Assuming all carriers are located in a single band, we can now specify the wave-vector and frequency integrals as

$$\int_k = k_F^3 \int \frac{d^3 \mathbf{K}}{(2\pi)^3} \quad \text{and} \quad \int_{\hbar\omega} = E_F \int d\Omega. \quad (\text{C1})$$

1. Collective mode drag term $G_{k,\omega}$

With these approximation, we can use Eq. (22) to write $T_{k,\omega}$ from Eq. (26) as

$$\begin{aligned} T_{k,\omega} = T_{K,\Omega} &= \frac{8\pi^2 e^2 / K^2}{\Im m(\varepsilon_{K,\Omega}^{\text{tot}})} \frac{1}{(2\pi)^3} \frac{k_F}{E_F} \\ &\times \int d^3 \mathbf{Q} \delta(|\mathbf{Q} + \mathbf{K}|^2 - Q^2 - \Omega) \\ &\times (f_Q^0 - f_{Q+K}^0) \frac{[\tau_{|Q+K|}(\mathbf{Q} + \mathbf{K}) - \tau_Q \mathbf{Q}] \cdot \mathbf{E}}{\mathbf{P} \cdot \mathbf{E}}. \end{aligned} \quad (\text{C2})$$

Here, we have used the Fourier transform of the Coulomb potential $v_k = \frac{4\pi e^2}{k^2 K^2}$. We evaluate the integral in Eq. (C2) in spherical coordinates, with the polar axis parallel to the \mathbf{K} direction and with the vectors \mathbf{K} and \mathbf{E} spanning the x - z plane.

That means that in Cartesian coordinates,

$$\begin{aligned} \mathbf{Q} &= Q \begin{pmatrix} \sin \theta \cos \varphi \\ \sin \theta \sin \varphi \\ \cos \theta \end{pmatrix}, \quad \mathbf{E} = E \begin{pmatrix} \sin \theta_{K,E} \\ 0 \\ \cos \theta_{K,E} \end{pmatrix}, \\ \mathbf{K} &= K \begin{pmatrix} 0 \\ 0 \\ 1 \end{pmatrix}, \end{aligned} \quad (\text{C3})$$

where Q , θ , and φ are the spherical coordinates of \mathbf{Q} and $\theta_{K,E}$ is the polar angle of \mathbf{E} , the angle between \mathbf{K} and \mathbf{E} . As none of the other factors in the integral depend on the azimuthal angle φ , we can evaluate the φ integral:

$$\frac{1}{2\pi} \int_0^{2\pi} d\varphi \mathbf{Q} \cdot \mathbf{E} = E \cdot \mathbf{K} \frac{Q}{K} \cos \theta. \quad (\text{C4})$$

We use the energy conservation delta-function to evaluate the θ integral, which means we can replace $\cos \theta$ by $\frac{\Omega - Q^2}{2QK}$, and eventually find

$$\begin{aligned} T_{K,\Omega} &= \frac{1}{\Im m(\varepsilon_{K,\Omega}^{\text{tot}})} \frac{e^2 k_F}{K^3 E_F} \int_{\frac{1}{2}|\frac{\Omega}{K} - K|}^{\infty} dQ Q (f_Q^0 - f_{\sqrt{Q^2 + \Omega}}^0) \\ &\times \frac{\tau_{\sqrt{Q^2 + \Omega}} (1 + \frac{\Omega}{K^2}) + \tau_Q (1 - \frac{\Omega}{K^2})}{2}. \end{aligned} \quad (\text{C5})$$

We split the integral for T into four parts:

$$\begin{aligned} T_{K,\Omega} &= \frac{1}{\Im m(\varepsilon_{K,\Omega}^{\text{tot}})} \frac{e^2 k_F}{K^3 E_F} \frac{1}{2} \left[\left(1 + \frac{\Omega}{K^2}\right) (I_{K,\Omega}^1 - I_{K,\Omega}^3) \right. \\ &\quad \left. + \left(1 - \frac{\Omega}{K^2}\right) (I_{K,\Omega}^2 - I_{K,\Omega}^4) \right] \end{aligned} \quad (\text{C6})$$

with

$$I_{K,\Omega}^1 = \int_{\frac{1}{2}|\frac{\Omega}{K} - K|}^{\infty} dQ Q f_Q^0 \tau_{\sqrt{Q^2 + \Omega}}, \quad (\text{C7})$$

$$I_{K,\Omega}^2 = \int_{\frac{1}{2}|\frac{\Omega}{K} - K|}^{\infty} dQ Q f_Q^0 \tau_Q. \quad (\text{C8})$$

By making the substitution $Q \rightarrow \sqrt{Q^2 + \Omega}$, we find that

$$I_{K,\Omega}^3 = \int_{\frac{1}{2}|\frac{\Omega}{K} - K|}^{\infty} dQ Q f_{\sqrt{Q^2 + \Omega}}^0 \tau_{\sqrt{Q^2 + \Omega}} = I_{K,-\Omega}^2, \quad (\text{C9})$$

$$I_{K,\Omega}^4 = \int_{\frac{1}{2}|\frac{\Omega}{K} - K|}^{\infty} dQ Q f_{\sqrt{Q^2 + \Omega}}^0 \tau_Q = I_{K,-\Omega}^1. \quad (\text{C10})$$

We exclusively use the expressions $I_{K,\pm\Omega}^1$ and $I_{K,\pm\Omega}^2$, and find

$$\begin{aligned} T_{K,\Omega} &= \frac{1}{\Im m(\varepsilon_{K,\Omega}^{\text{tot}})} \frac{e^2 k_F}{K^3 E_F} \\ &\times \frac{1}{2} \left\{ (I_{K,\Omega}^1 - I_{K,-\Omega}^1) + (I_{K,\Omega}^2 - I_{K,-\Omega}^2) \right. \\ &\quad \left. + \frac{\Omega}{K^2} [(I_{K,\Omega}^1 + I_{K,-\Omega}^1) - (I_{K,\Omega}^2 + I_{K,-\Omega}^2)] \right\}, \end{aligned} \quad (\text{C11})$$

which, together with the antisymmetry in Ω of $\Im m(\varepsilon_{K,\Omega}^{\text{tot}})$ shows that $T_{K,-\Omega} = T_{K,\Omega}$.

2. Effective momentum relaxation time τ_p

Let us evaluate Eq. (27) for spherical parabolic bands. In the dimensionless variables from Sec. C1, the integral reads

$$\frac{1}{\tau_p} = \frac{k_F^3}{(2\pi)^3} \int d^3\mathbf{K} \int d\Omega W_{\mathbf{K},\Omega}^0 \delta(|\mathbf{P} + \mathbf{K}|^2 - P^2 - \Omega) \frac{f_{|\mathbf{P}+\mathbf{K}|}^0}{f_P^0} \times (N_\Omega^0 + 1) \left[1 - \frac{\tau_{|\mathbf{P}+\mathbf{K}|}}{\tau_p} \frac{(\mathbf{P} + \mathbf{K}) \cdot \mathbf{E}}{\mathbf{P} \cdot \mathbf{E}} + \frac{T_{\mathbf{K},\Omega}}{\tau_p} \frac{\mathbf{K} \cdot \mathbf{E}}{\mathbf{P} \cdot \mathbf{E}} \right]. \quad (\text{C12})$$

As in Sec. C1, we will solve this integral in spherical coordinates. Alignment of the coordinate system is identical to that in Sec. C1, except for the naming to the vectors, i.e., Eqs. (C3) and (C4) hold, if we set $\mathbf{K} \rightarrow \mathbf{P}$ and $\mathbf{Q} \rightarrow \mathbf{K}$:

$$\frac{1}{2\pi} \int_0^{2\pi} d\varphi \mathbf{K} \cdot \mathbf{E} = \mathbf{E} \cdot \mathbf{P} \frac{K}{P} \cos \theta. \quad (\text{C13})$$

We also need to assume that $T_{\mathbf{K},\Omega} = T_{K,\Omega}$, which is another way of requiring that $\Im(\varepsilon_{\mathbf{K},\Omega}^{\text{tot}}) = \Im(\varepsilon_{K,\Omega}^{\text{tot}})$. On inspecting Eq. (18), we see that this is consistent with our assumption of spherical bands. Furthermore, we need $W_{\mathbf{K},\Omega}^0 = W_{K,\Omega}^0$, which means that the real part of the dielectric function cannot depend on the direction of the wave vector either, $\Re(\varepsilon_{\mathbf{K},\Omega}^{\text{tot}}) = \Re(\varepsilon_{K,\Omega}^{\text{tot}})$, see Eq. (10).

Hence we can carry out the integral over the azimuthal and polar angles in Eq. (C12). Using the delta function in Eq. (C12), we can set $\cos \theta = \frac{\Omega - K^2}{2PK}$ yielding

$$\frac{1}{\tau_p} = \frac{k_F^3}{(2\pi)^2} \frac{1}{2P} \int_0^\infty dK K \times \int_{K(K-2P)}^{K(K+2P)} d\Omega W_{K,\Omega}^0 \frac{f_{\sqrt{P^2+\Omega}}^0}{f_P^0} (N_\Omega^0 + 1) \times \left[1 - \frac{\tau_{\sqrt{P^2+\Omega}}}{\tau_p} \left(1 + \frac{\Omega - K^2}{2P^2} \right) + \frac{T_{K,\Omega}}{\tau_p} \frac{\Omega - K^2}{2P^2} \right]. \quad (\text{C14})$$

From Eq. (C14), we can read that an infinite mobility solution of the type discussed in Sec. IID3 holds if $\tau_p = T_{K,\Omega} = \text{const.}$

Quasielastic relaxation time approximation. As discussed in Sec. IID3, for the initial step $n = 1$ in our iteration, we set $\tau_p^0 = \tau = \text{const.}$ and we assume $|\mathbf{P} + \mathbf{K}| \approx P$ in the square bracket in Eq. (C14), so that it will be replaced by $(1 - \frac{\cos \theta_{\mathbf{P}+\mathbf{K},\mathbf{E}}}{\cos \theta_{\mathbf{P},\mathbf{E}}})$, where $\theta_{A,B}$ is the angle between \mathbf{A} and \mathbf{B} . This approximation is only made in this term, that is, Ω is not set to zero anywhere else in Eq. (C14). When we integrate over the azimuthal angle,

$$\frac{1}{2\pi} \int_0^{2\pi} d\varphi \left(1 - \frac{\cos \theta_{\mathbf{P}+\mathbf{K},\mathbf{E}}}{\cos \theta_{\mathbf{P},\mathbf{E}}} \right) = 1 - \cos \theta_{\mathbf{P}+\mathbf{K},\mathbf{P}} \geq 0, \quad (\text{C15})$$

we see that the quasielastic scattering approximation ensures that τ_p^1 is non-negative, independent of the particulars of the scattering mechanism. Consequently, the quasielastic relaxation time for materials with spherical parabolic bands

reads

$$\frac{1}{\tau_p^{1,e}} = \frac{k_F^3}{(2\pi)^2} \frac{1}{2P} \int_0^\infty dK K \times \int_{K(K-2P)}^{K(K+2P)} d\Omega W_{K,\Omega}^0 \frac{f_{\sqrt{P^2+\Omega}}^0}{f_P^0} (N_\Omega^0 + 1) \times \left[1 - \frac{P}{\sqrt{P^2+\Omega}} \left(1 + \frac{\Omega - K^2}{2P^2} \right) \right]. \quad (\text{C16})$$

APPENDIX D: EFFECTIVE MOMENTUM RELAXATION TIME FOR MATERIALS WITH SPHERICAL PARABOLIC BANDS: 2D

1. Integration of the inverse square root singularities

As we will see, in the two-dimensional case, the integrals in the Boltzmann equation can have inverse square root singularities at both the upper and the lower integration limits. Yet, integrals of the type

$$I = \int_{\Omega_{\min}}^{\Omega_{\max}} d\Omega \frac{g(\Omega)}{\sqrt{\Omega - \Omega_{\min}} \sqrt{\Omega_{\max} - \Omega}} \quad (\text{D1})$$

are integrable unless the function $g(\Omega)$ introduces difficulties (see, e.g., Ref. [57]). To see this, we start by splitting I at some Ω_{mid} with $\Omega_{\min} < \Omega_{\text{mid}} < \Omega_{\max}$. For the lower part of the integral, we make the substitution $t = \sqrt{\Omega - \Omega_{\min}}$:

$$I_1 = \int_{\Omega_{\min}}^{\Omega_{\text{mid}}} d\Omega \frac{g(\Omega)}{\sqrt{\Omega - \Omega_{\min}} \sqrt{\Omega_{\max} - \Omega}} = \int_0^{\sqrt{\Omega_{\text{mid}} - \Omega_{\min}}} dt \frac{2g(\Omega_{\min} + t^2)}{\sqrt{\Omega_{\max} - \Omega_{\min} - t^2}}. \quad (\text{D2})$$

Our choice of Ω_{mid} guarantees that the remaining inverse square root in Eq. (D2) does not become singular.

Similarly, we make the substitution $t = \sqrt{\Omega_{\max} - \Omega}$ for the upper part of the integral:

$$I_2 = \int_{\Omega_{\text{mid}}}^{\Omega_{\max}} d\Omega \frac{g(\Omega)}{\sqrt{\Omega - \Omega_{\min}} \sqrt{\Omega_{\max} - \Omega}} = \int_0^{\sqrt{\Omega_{\max} - \Omega_{\text{mid}}}} dt \frac{2g(\Omega_{\max} - t^2)}{\sqrt{\Omega_{\max} - \Omega_{\min} - t^2}}. \quad (\text{D3})$$

The integral I is the sum of I_1 and I_2 .

2. Integrals for momentum relaxation time

In dimensionless variables, the integral for the momentum relaxation time reads

$$\frac{1}{\tau_p} = \frac{k_F^2}{(2\pi)^2} \int d^2\mathbf{K} \int d\Omega W_{\mathbf{K},\Omega}^0 \delta(|\mathbf{P} + \mathbf{K}|^2 - P^2 - \Omega) \times \left[1 - \frac{\tau_{|\mathbf{P}+\mathbf{K}|}}{\tau_p} \frac{(\mathbf{P} + \mathbf{K}) \cdot \mathbf{E}}{\mathbf{P} \cdot \mathbf{E}} + \frac{T_{\mathbf{K},\Omega}}{\tau_p} \frac{\mathbf{K} \cdot \mathbf{E}}{\mathbf{P} \cdot \mathbf{E}} \right] \times \frac{f_{|\mathbf{P}+\mathbf{K}|}^0}{f_P^0} (N_\Omega^0 + 1) \quad (\text{D4})$$

if we assume that all carriers are located in the $z = 0$ plane and hence all transferred wave vectors \mathbf{K} are also truly two-dimensional. We also neglect intervalley scattering. We

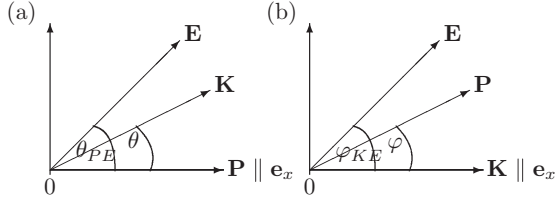


FIG. 19. Coordinate system for (a) \mathbf{K} integral in τ_P , Eq. (D4), and (b) \mathbf{P} integral in $T_{K,\Omega}$, Eq. (D10).

carry out the integral over \mathbf{K} in two-dimensional cylindrical coordinates with the x-axis aligned with \mathbf{P} , as in Fig. 19(a). The angle between \mathbf{P} and \mathbf{K} is the integration variable θ , and the angle between \mathbf{P} and \mathbf{E} is θ_{PE} . As in the three-dimensional case, we assume that $W_{K,\Omega} = W_{K,\Omega}$. The delta function reads

$$\delta(|\mathbf{P} + \mathbf{K}|^2 - P^2 - \Omega) = \frac{1}{2PK} \delta\left(\cos\theta - \frac{\Omega - K^2}{2PK}\right)$$

and

$$|\mathbf{P} + \mathbf{K}| = \sqrt{P^2 + K^2 + 2PK \cos\theta}.$$

So far, all terms have been symmetric in the angle θ . The term

$$\frac{\mathbf{K} \cdot \mathbf{E}}{\mathbf{P} \cdot \mathbf{E}} = \frac{K \cos(\theta_{PE} - \theta)}{P \cos\theta_{PE}} = \frac{K}{P} \cos\theta + \frac{K}{P} \tan\theta_{PE} \sin\theta \quad (\text{D5})$$

has an antisymmetric contribution. The θ integral over the antisymmetric summand vanishes:

$$\begin{aligned} \int_{-\pi}^{\pi} d\theta h(\theta) &= \int_0^{\pi} d\theta [h(\theta) + h(-\theta)] \\ &= \begin{cases} 0 & h(-\theta) = -h(\theta), \\ 2 \int_0^{\pi} d\theta h(\theta) & h(-\theta) = h(\theta). \end{cases} \quad (\text{D6}) \end{aligned}$$

Eventually, this yields

$$\begin{aligned} \frac{1}{\tau_P} &= \frac{k_F^2}{(2\pi)^2} \int_0^{\infty} dK K \int_{K(K-2P)}^{K(K+2P)} d\Omega \\ &\times \frac{2W_{K,\Omega}^0(N_{\Omega}^0 + 1)}{\sqrt{\Omega - K(K-2P)}\sqrt{K(K+2P) - \Omega}} \frac{f_{\sqrt{P^2+\Omega}}^0}{f_P^0} \\ &\times \left[1 - \frac{\tau_{\sqrt{P^2+\Omega}}}{\tau_P} \left(1 + \frac{\Omega - K^2}{2P^2} \right) + \frac{T_{K,\Omega}}{\tau_P} \frac{\Omega - K^2}{2P^2} \right]. \quad (\text{D7}) \end{aligned}$$

Here we used that the integral over θ is

$$\begin{aligned} \int_0^{\pi} d\theta \frac{1}{2PK} \delta\left(\cos\theta - \frac{\Omega - K^2}{2PK}\right) \\ = \begin{cases} \frac{1}{\sqrt{\Omega - K(K-2P)}\sqrt{K(K+2P) - \Omega}} & K(K-2P) \leq \Omega \leq K(K+2P), \\ 0 & \text{else.} \end{cases} \quad (\text{D8}) \end{aligned}$$

For the quasielastic momentum relaxation time from Eq. (30), we have to replace the square bracket in Eq. (D7) with its quasielastic, RTA limit. This bracket turns out to be

identical to its 3D equivalent, so that Eq. (30) becomes

$$\begin{aligned} \frac{1}{\tau_P} &= \frac{k_F^2}{(2\pi)^2} \int_0^{\infty} dK K \int_{K(K-2P)}^{K(K+2P)} d\Omega \\ &\times \frac{2(N_{\Omega}^0 + 1)}{\sqrt{\Omega - K(K-2P)}\sqrt{K(K+2P) - \Omega}} \\ &\times \frac{f_{\sqrt{P^2+\Omega}}^0}{f_P^0} \left[1 - \frac{P}{\sqrt{P^2 + \Omega}} \left(1 + \frac{\Omega - K^2}{2P^2} \right) \right] W_{K,\Omega}^0 C_{K,\Omega}. \quad (\text{D9}) \end{aligned}$$

3. Integrals for phonon drag term

With dimensionless variables the 2D phonon drag Eq. (26) reads

$$\begin{aligned} T_{K,\Omega} &= \frac{2\pi \nu_K k_F^2}{\Im(\varepsilon_{K,\Omega}^{\text{tot}}) E_F} \frac{M_v}{(2\pi)^2} \int d\mathbf{P}^2 \delta(|\mathbf{K} + \mathbf{P}|^2 - |\mathbf{P}|^2 - \Omega) \\ &\times (f_{|\mathbf{P}|}^0 - f_{|\mathbf{K}+\mathbf{P}|}^0) \frac{\tau_{|\mathbf{P}+\mathbf{K}|}(\mathbf{P} + \mathbf{K}) \cdot \mathbf{E} - \tau_{|\mathbf{P}|} \mathbf{P} \cdot \mathbf{E}}{\mathbf{K} \cdot \mathbf{E}}. \quad (\text{D10}) \end{aligned}$$

Here, $\nu_K = \frac{2\pi e^2}{k_F K}$ is the Fourier transform of the Coulomb integral in two-dimensional space, which we can use because we assume all carriers are located in the $z = 0$ plane. The factor M_v is a scalar accounting for the possibility of multiple degenerate valleys. With several degenerate valleys, there are n_S/M_v carriers in each valley, and the carrier dielectric function is M_v times the contribution of a single valley.

We orient the coordinate system with $\mathbf{K} \parallel \mathbf{e}_x$, see Fig. 19(b). This means that

$$\frac{\mathbf{P} \cdot \mathbf{E}}{\mathbf{K} \cdot \mathbf{E}} = \frac{P}{K} (\cos\varphi + \sin\varphi \tan\varphi_E)$$

with φ and φ_E defined in Fig. 19(b). As the terms with $\sin\varphi$ cancel due to antisymmetry [see Eq. (D6)], we can write

$$\begin{aligned} T_{K,\Omega} &= \frac{M_v e^2 k_F}{E_F K^2 \Im(\varepsilon_{K,\Omega}^{\text{tot}})} \int_{|\frac{\Omega-K^2}{2K}|}^{\infty} dP P \frac{f_P^0 - f_{\sqrt{P^2+\Omega}}^0}{\sqrt{P^2 - (\frac{\Omega-K^2}{2K})^2}} \\ &\times \frac{1}{2} \left[\tau_{\sqrt{P^2+\Omega}} \left(1 + \frac{\Omega}{K^2} \right) + \tau_P \left(1 - \frac{\Omega}{K^2} \right) \right]. \quad (\text{D11}) \end{aligned}$$

Here we have used $\nu_K = \frac{2\pi e^2}{k} = \frac{2\pi e^2}{K k_F}$. We define

$$I_{K,\Omega}^1 = \int_{|\frac{\Omega-K^2}{2K}|}^{\infty} dP P \frac{f_P^0 \tau_{\sqrt{P^2+\Omega}}}{\sqrt{P^2 - (\frac{\Omega-K^2}{2K})^2}}, \quad (\text{D12})$$

$$I_{K,\Omega}^2 = \int_{|\frac{\Omega-K^2}{2K}|}^{\infty} dP P \frac{f_P^0 \tau_P}{\sqrt{P^2 - (\frac{\Omega-K^2}{2K})^2}}, \quad (\text{D13})$$

$$I_{K,\Omega}^3 = \int_{|\frac{\Omega-K^2}{2K}|}^{\infty} dP P \frac{f_{\sqrt{P^2+\Omega}}^0 \tau_{\sqrt{P^2+\Omega}}}{\sqrt{P^2 - (\frac{\Omega-K^2}{2K})^2}}, \quad (\text{D14})$$

$$I_{K,\Omega}^4 = \int_{|\frac{\Omega-K^2}{2K}|}^{\infty} dP P \frac{f_{\sqrt{P^2+\Omega}}^0 \tau_P}{\sqrt{P^2 - (\frac{\Omega-K^2}{2K})^2}}, \quad (\text{D15})$$

With the substitution $P \rightarrow P' = \sqrt{P^2 - \Omega}$, one can see that $I_{K,\Omega}^3 = I_{K,-\Omega}^2$ and $I_{K,\Omega}^4 = I_{K,-\Omega}^1$. Using $\frac{e^2 k_F}{E_F} = \frac{2}{k_F a_0}$ yields

$$T_{K,\Omega} = \frac{M_v}{k_F a_0 K^2 \Im(\varepsilon_{K,\Omega}^{\text{tot}})} \left\{ I_{K,\Omega}^1 - I_{K,-\Omega}^1 + I_{K,\Omega}^2 - I_{K,-\Omega}^2 + \frac{\Omega}{K^2} [I_{K,\Omega}^1 + I_{K,-\Omega}^1 - (I_{K,\Omega}^2 + I_{K,-\Omega}^2)] \right\}. \quad (\text{D16})$$

The $I_{K,\Omega}^i$ are all integrals of the type of Eq. (D2), that means the singularity at $P = P_{\min} = |\frac{\Omega - K^2}{2K}|$ is integrable. When implementing the numerical evaluation of these integrals, the value of $T_{K,\Omega}$ for constant τ ,

$$T_{K,\Omega}|_{\tau=\text{const}} = \frac{\Im(\varepsilon_{K,\Omega}^e)}{\Im(\varepsilon_{K,\Omega}^{\text{tot}})} \tau \quad (\text{D17})$$

can be helpful as a test.

APPENDIX E: OTHER SCATTERING MECHANISMS IN MoS₂ HETEROSTRUCTURES

Other than interface phonon-plasmon scattering, we consider scattering mechanisms which are intrinsic to the investigated structure, that is, acoustic and optical deformation potential scattering (ADP and ODP) and piezoelectric scattering (PE). We use parameters for relaxation times Kaasbjerg *et al.* [26,29] calculated for a monolayer of MoS₂ in a vacuum, cf. Table III.

1. Acoustic deformation potential scattering and piezoelectric scattering

We treat ADP scattering and PE scattering as elastic processes. We also neglect interference term between ADP and PE, so that each process has an independent momentum relaxation time [[26], Sec. C2]. For a carrier with momentum

TABLE III. Material parameters for MoS₂.^a

Quantity	Symbol	Value
Effective mass	m^*	$0.35 m_e^b$
Ion mass sheet density	ρ	$3.17 \times 10^{-7} \frac{\text{g}}{\text{cm}^2}$
LA speed of sound	c_{LA}	$6.7 \times 10^5 \frac{\text{cm}}{\text{s}}$
TA speed of sound	c_{TA}	$4.2 \times 10^5 \frac{\text{cm}}{\text{s}}$
LA ADP	Ξ_{LA}	2.4 eV
TA ADP	Ξ_{TA}	1.5 eV
PE effective ADP	Ξ_{PE}	2.39 eV ^c
LO-phonon energy	$\hbar\omega_{LO}$	47.9 meV ^d
Homopolar phonon energy	$\hbar\omega_{HP}$	50.0 meV
LO ODP	D_{LO}	$2.6 \times 10^8 \frac{\text{eV}}{\text{cm}}^e$
HP ODP	D_{HP}	$4.1 \times 10^8 \frac{\text{eV}}{\text{cm}}^e$

^aFrom Ref. [26] unless a different reference is given.

^bReference [23].

^cCalculated with Ref. [[26], Eq. (15)].

^dReference [48].

^eReference [29].

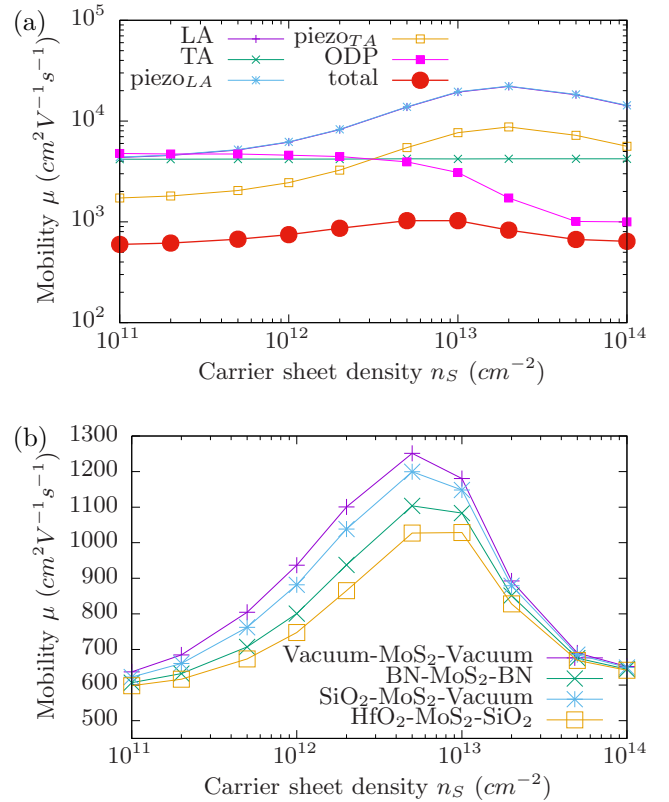


FIG. 20. Room-temperature mobility as a function of carrier sheet density with all intrinsic scattering mechanisms considered, except for interface phonon-plasmon scattering. (a) Room-temperature mobility due to acoustic deformation potential scattering of the LA and TA modes, piezoelectric scattering of the LA and TA modes, and zero-order optical deformation potential scattering, and the total mobility resulting from all these scattering mechanisms for the HfO₂-MoS₂-SiO₂ structure. (b) Total room temperature mobility due to acoustic and optical deformation potential scattering and piezoelectric scattering in the different investigated structures marked.

p , the momentum relaxation rate is [26,29]

$$\frac{1}{\tau_p} = \frac{\Xi^2 m^* k_B T}{\hbar^3 \rho c} \frac{1}{\pi} \int_0^\pi d\varphi \frac{1 - \cos \varphi}{|\tilde{\varepsilon}_{k(\varphi), \omega=0}|^2}, \quad (\text{E1})$$

where $k(\varphi) = \sqrt{2p(1 - \cos \varphi)}$ is the magnitude of the transferred wave vector if the angle between the initial and final wave vectors is φ . m^* and ρ are the effective mass and ion mass sheet density of MoS₂. c is the speed of sound of the TA or LA phonon, and Ξ is the corresponding ADP, or effective long-wavelength piezoelectric potential (see Eq. (15) in Ref. [26]).

$\tilde{\varepsilon}_{k,\omega}$ is the free carrier contribution to the static dielectric function of the structure. The screening due to the valence electrons is already taken into account in the deformation potential [[26], Sec. C2]. Hence

$$\tilde{\varepsilon}_{k,\omega=0} = 1 + \frac{2\pi k \chi_{k,\omega=0}}{\varepsilon_{k,\omega=0}^{\text{interface}}}, \quad (\text{E2})$$

where $\varepsilon_{k,\omega}^{\text{interface}}$ is the static dielectric function of the structure, Eq. (51) and $\chi_{k,\omega}$ is the free electron susceptibility from Eq. (55). As $\varepsilon_{k,\omega}^{\text{interface}}$ enters, the screening is different for differ-

ent structures, see Fig. 20(b). Ma and Jena, Kaasbjerg *et al.*, and Bogulsawski *et al.* [25,26] agree that the TA ADP should have $\bar{\varepsilon} = 1$. Kaasbjerg *et al.* make the argument that this is because TA ADP scattering is dominated by umklapp processes, which should be unscreened by free carriers. Bogulsawski *et al.* [58,59] argue that in the long-wavelength limit, this result follows from the symmetry of the TA ADP matrix element in a semiconductor with multiple spherical valleys like MoS₂.

2. Optical deformation potential scattering

ODP scattering is an inelastic process. The momentum relaxation time is (see Eq. (31) in Ref. [29])¹⁰

$$\frac{1}{\tau_p} = \frac{m^* D^2}{2\hbar^2 \rho \omega} [N_\omega^0 + (N_\omega^0 + 1) \Theta(E_p - \hbar\omega)]. \quad (\text{E3})$$

Here, D is the zeroth-order ODP due to the LO or homopolar mode of constant frequency ω . The Heaviside step function Θ makes sure the emission term vanishes when the electron energy is smaller than the phonon energy. First-order ODP and

intervalley ADP have been found to be insignificant for low field transport [29] and will be neglected.

3. LO-phonon scattering

The scattering due to the Fröhlich interaction in Kaasbjerg *et al.* [29] is of an interface phonon type, not of a confined phonon type, as can be seen from their discussion in Ref. [[29], Appendix B]. Ma and Jena [25] include Fröhlich scattering of the interface or remote phonon type and of the confined phonon type (which they refer to as LO-phonon scattering).¹¹ This is not double counting. In fact, the Poisson equation has solutions of confined and of interface type [60,61]. However, the confinement in a slab of MoS₂ with a thickness of $a = 6.145 \text{ \AA}$ is so strong that confined solutions do not contribute to low-field transport. The discretized wave vectors allowed for the confined modes would be $k_n = n\frac{\pi}{a} \approx n 5.1 \times 10^7 \text{ cm}^{-1}$, which means that even k_1 is roughly three times larger than the Fermi wave vector for the largest carrier concentrations considered, $k_F(n_s = 10^{14} \text{ cm}^{-2}) \approx 1.8 \times 10^7 \text{ cm}^{-1}$.

¹⁰ODP is not screened by free carriers in MoS₂ due to the symmetry of the ODP [58].

¹¹However, despite the confined nature of these modes, Ma and Jena [25] screen them as if they were interface type modes.

-
- [1] P. D.-C. Marisol Martin-Gonzalez and O. Caballero-Calero, *Renew. Sustain. Energy Rev.* **24**, 288 (2013).
 - [2] K. S. Novoselov, D. Jiang, F. Schedin, T. J. Booth, V. V. Khotkevich, S. V. Morozov, and A. K. Geim, *Proc. Natl. Acad. Sci. USA* **102**, 10451 (2005).
 - [3] B. Radisavljevic, A. Radenovic, J. Brivio, V. Giacometti, and A. Kis, *Nat. Nano* **6**, 147 (2011).
 - [4] F. Rossi and T. Kuhn, *Rev. Mod. Phys.* **74**, 895 (2002).
 - [5] J. Shah, *Ultrafast Spectroscopy of Semiconductors and Semiconductor Nanostructures*, Springer Series in Solid-State Sciences (Springer, Berlin, Heidelberg, 2013).
 - [6] C. M. Wolfe, G. E. Stillman, and W. T. Lindley, *J. Appl. Phys.* **41**, 3088 (1970).
 - [7] B. A. Sanborn, *Phys. Rev. B* **51**, 14247 (1995).
 - [8] J. M. Ziman, *Electrons and Phonons* (Oxford University Press, Oxford, 1962).
 - [9] A. Mooradian and G. B. Wright, *Phys. Rev. Lett.* **16**, 999 (1966).
 - [10] B. B. Varga, *Phys. Rev.* **137**, A1896 (1965).
 - [11] M. E. Kim, A. Das, and S. D. Senturia, *Phys. Rev. B* **18**, 6890 (1978).
 - [12] B. K. Ridley, *Quantum Processes in Semiconductors*, 4th ed. (Clarendon Press, Oxford, 1999).
 - [13] M. V. Fischetti, D. A. Neumayer, and E. A. Cartier, *J. Appl. Phys.* **90**, 4587 (2001).
 - [14] R. A. Cowley and G. Dolling, *Phys. Rev. Lett.* **14**, 549 (1965).
 - [15] J. Lindhard, Kgl. Danske Videnskab. Selskab, Mat.-fys. Medd. **28** (1954).
 - [16] R. H. Lyddane, R. G. Sachs, and E. Teller, *Phys. Rev.* **59**, 673 (1941).
 - [17] B. A. Sanborn, *Phys. Rev. B* **51**, 14256 (1995).
 - [18] R. E. Peierls, *Quantum Theory of Solids* (Clarendon Press, Oxford, 1955).
 - [19] K. Hess and P. Vogl, *Solid State Commun.* **30**, 797 (1979).
 - [20] D. L. Maslov, *Phys. Rev. B* **45**, 1911 (1992).
 - [21] F. Stern, *Phys. Rev. Lett.* **18**, 546 (1967).
 - [22] K. F. Mak, C. Lee, J. Hone, J. Shan, and T. F. Heinz, *Phys. Rev. Lett.* **105**, 136805 (2010).
 - [23] T. Cheiwchanchamnangij and W. R. L. Lambrecht, *Phys. Rev. B* **85**, 205302 (2012).
 - [24] B. Radisavljevic and A. Kis, *Nat. Mater.* **12**, 815 (2013).
 - [25] N. Ma and D. Jena, *Phys. Rev. X* **4**, 011043 (2014).
 - [26] K. Kaasbjerg, K. S. Thygesen, and A.-P. Jauho, *Phys. Rev. B* **87**, 235312 (2013).
 - [27] L. Zeng, Z. Xin, S. Chen, G. Du, J. Kang, and X. Liu, *Appl. Phys. Lett.* **103**, 113505 (2013).
 - [28] Z.-Y. Ong and M. V. Fischetti, *Phys. Rev. B* **88**, 165316 (2013).
 - [29] K. Kaasbjerg, K. S. Thygesen, and K. W. Jacobsen, *Phys. Rev. B* **85**, 115317 (2012).
 - [30] D. Pines, *Elementary Excitations in Solids: Lectures on Protons, Electrons, and Plasmons* (Benjamin, New York, 1964).
 - [31] P. Nozieres and D. Pines, *Theory of Quantum Liquids*, Advanced Books Classics Series (Westview, Boulder, CO, 1999).
 - [32] H. Nyquist, *Phys. Rev.* **32**, 110 (1928).
 - [33] H. B. Callen and T. A. Welton, *Phys. Rev.* **83**, 34 (1951).
 - [34] K. Fletcher and P. N. Butcher, *J. Phys. C: Solid State Phys.* **5**, 212 (1972).
 - [35] P. Yu and M. Cardona, *Fundamentals of Semiconductors: Physics and Materials Properties*, Advanced Texts in Physics, Vol. 3 (Springer, New York, 2005).
 - [36] N. R. Arista and W. Brandt, *Phys. Rev. A* **29**, 1471 (1984).
 - [37] B. Y.-K. Hu and K. Flensberg, *Phys. Rev. B* **53**, 10072 (1996).

- [38] G. Mahan, *Many Particle Physics*, Physics of Solids and Liquids (Kluwer Academic/Plenum Publishers, New York/Boston, 2000).
- [39] L. Landau, JETP **16**, 574 (1946), translated from Russian by E. Lifschitz.
- [40] M. Bleicher, *Halbleiter-Optoelektronik* (Hüthig, Heidelberg, 1986).
- [41] S. Perkowitz, *Phys. Rev. B* **12**, 3210 (1975).
- [42] B. Laikhtman and P. M. Solomon, *Phys. Rev. B* **72**, 125338 (2005).
- [43] K. Flensberg and B. Y.-K. Hu, *Phys. Rev. B* **52**, 14796 (1995).
- [44] B. Laikhtman and P. M. Solomon, *J. Appl. Phys.* **103**, 014501 (2008).
- [45] A. L. Fetter, *Phys. Rev. B* **10**, 3739 (1974).
- [46] P. F. Maldague, *Surf. Sci.* **73**, 296 (1978).
- [47] R. Geick, C. H. Perry, and G. Rupprecht, *Phys. Rev.* **146**, 543 (1966).
- [48] T. J. Wieting and J. L. Verble, *Phys. Rev. B* **3**, 4286 (1971).
- [49] F. Gervais and B. Piriou, *Phys. Rev. B* **11**, 3944 (1975).
- [50] A. I. Kasiyan and P. I. Russu, *Phys. Status Solidi (b)* **128**, 243 (1985).
- [51] T. Gunst, T. Markussen, K. Stokbro, and M. Brandbyge, *Phys. Rev. B* **93**, 035414 (2016).
- [52] A. Molina-Sánchez and L. Wirtz, *Phys. Rev. B* **84**, 155413 (2011).
- [53] Y. Cai, J. Lan, G. Zhang, and Y.-W. Zhang, *Phys. Rev. B* **89**, 035438 (2014).
- [54] D. Y. Qiu, F. H. da Jornada, and S. G. Louie, *Phys. Rev. Lett.* **111**, 216805 (2013).
- [55] N. W. Ashcroft and N. D. Mermin, *Solid State Physics* (Saunders College, Philadelphia, 1976).
- [56] M. Combescot and R. Combescot, *Phys. Rev. B* **35**, 7986 (1987).
- [57] W. H. Press, S. A. Teukolsky, W. T. Vetterling, and B. P. Flannery, *Numerical Recipes in C: The Art of Scientific Computing*, 2nd ed. (Cambridge University Press, New York, 1992).
- [58] P. Boguslawski, *J. Phys. C: Solid State Phys.* **10**, L417 (1977).
- [59] P. Bogulsawski and J. Mycielski, *J. Phys. C: Solid State Phys.* **10**, 2413 (1977).
- [60] K. J. Nash, *Phys. Rev. B* **46**, 7723 (1992).
- [61] M. A. Stroscio and M. Dutta, *Phonons in Nanostructures*, 1st ed. (Cambridge University Press, Cambridge, 2001).